Liquid Metal Embrittlement in Resistance Spot Dissimilar Welds on Advanced High Strength Steels:

Microstructure and Fracture Characteristic

Undergraduate Research Thesis

Presented in Partial Fulfillment of the Requirements for Graduation with Research Distinction in the College of Engineering of The Ohio State University

Prepared by: Michael B. Stotts

Welding Engineering Program

The Ohio State University

2018

Defense Committee:

Dr. Carolin Fink

Dr. Antonio Ramirez

Liquid Metal Embrittlement in Resistance Spot Dissimilar Welds on Advanced High Strength Steels: Microstructure and Fracture Characteristic

Approved by:

Dr. Carolin Fink, Advisor
Department of Material Science
The Ohio State University

Dr. Antonio Ramirez
Department of Material Science
The Ohio State University

Date Approved: November 21, 2018

ACKNOWLEDGEMENTS

So many thanks to give to so many people. To my friends and family, all of you who supported me. Dr. Carolin Fink for her continued support throughout all this project's trials and tribulations, her willingness to let me try and fail on my own, and her vast amount of knowledge. Professor Menachim Kimchi for the materials for this project and expertise in Resistance Spot Welding. Isaac Luther for all his help with the welding equipment. Alex Martin for help with the 3-D modeling and printing process. Dean Sage for help with electro-galvanization process. Louie Aguilar for help with weld testing, spectrometry work, and SEM analysis.

TABLE OF CONTENTS

LIST OF TABLES

LIST OF FIGURES

LIST OF SYMBOLS AND ABBREVIATIONS

AC	ALTERNATING CURRENT
AHSS	ADVANCED HIGH STRENGTH STEEL
BSE	BACKSCATTERED ELECTRONS
DC	DIRECT CURRENT
DOT	DEPARTMENT OF TRANSPORTATION
DP	DUAL PHASE
EDS	ENERGY DISPERSED X-RAY SPECTROSCOPY
EPA	ENVIRONMENTAL PROTECTION AGENCY
FZ	FUSION ZONE
GMAW	GAS METAL ARC WELDING
GTAW	GAS TUNSGTEN ARC WELDING
HAZ	HEAT AFFECTED ZONE
I	CURRENT
J	JOULE HEATING
LME	LIQUID METAL EMBRITTLEMENT
LOM	LIGHT OPTICAL MICRCOSCOPY
MFDC	MID-FREQUENCY DIRECT CURRENT
MPG	MILES PER GALLON
P	RESISTIVITY
PHBS	PRESS-HARDENED BORON STEEL
R	RESISTANCE
RSW	RESISTANCE SPOT WELDER

SEM	SCANNING ELECTRON MICROSCOPE
T	TIME
TRIP	TRANSFORMATION INDUCED PLASTICITY
TWIP	TWINNING INDUCED PLASTICITY

LIST OF EQUATIONS

1) $$J = I^2Rt$$

2) $$R = \frac{\rho l}{A}$$

ABSTRACT

Advanced High Strength Steels (AHSS) are being utilized in automotive production in an effort for body-in- white weight reduction while being able to attain an increase in structural strength. During the Resistance Spot Welding (RSW) of these AHSS in dissimilar metal combinations such as with Zinc (Zn) coated low alloy steels, it is believed that liquid Zn penetrates along the grain boundaries in the Heat Affected Zone (HAZ), resulting in the embrittlement of the AHSS and subsequent cracking, a phenomenon known as Liquid Metal Embrittlement (LME). Although widely studied, the mechanisms behind LME are still not well understood.

The objectives of this research are to (1) reproduce LME induced cracking in a laboratory environment, (2) develop procedures for the metallographic examination of the cracks, and (3) characterize the cracking morphology (e.g. crack location, crack path, fracture surface) to identify the weld microstructures susceptible to LME. The resistance spot welding process will be varied in terms of welding parameters and the application of additional stresses during welding to introduce LME induced cracking. Metallographic evaluation includes light optical microscopy and scanning electron microscopy.

The testing involved three different AHSS including two Dual Phase (DP) steels (DP590, DP980) and a Press-Hardened Boron Steel (PHBS) Usibor-1500 in dissimilar metal combination with a Zn-galvanized low alloy steel. Results revealed that varying weld parameters alone were unsuccessful at reproducing LME cracking in the laboratory setting. With the introduction of external tensile strains using an offset electrode setup, cracking was achieved in the HAZ of all three base metals.

Although not enough samples were produced so far to conclusively determine which microstructures are most susceptible to LME cracking, the results agreed with previous research on LME, such that cracking occurred in the HAZ of the welds with an intergranular crack path.

CHAPTER 1. INTRODUCTION

Current Environment Protection Agency (EPA) fuel economy standards miles per gallon (mpg) requirements for domestically manufactured vehicles are increasing with the average goal of 51.3 mpg by 2025 (1). To satisfy these requirements, the automotive industry is looking to body-in-white weight reduction as a partial solution. Advanced high-strength steels (AHSS) are being increasingly used in the automotive to assist in weight reduction, safety performance improvement, and cost savings. These AHSS are implemented into existing car body structures, using resistance spot welding, which is the most commonly used welding process in the automotive vehicle assembly industry. This requires these steels to be welded in dissimilar metals welds. In many cases, this involves galvanized steels, which are used to prevent external corrosion of the car body. Experiences with these dissimilar metal welds show that in some cases cracking occurs in the Heat-Affected Zone (HAZ) of the AHSS due to Liquid Metal Embrittlement (LME). LME cracking can occur on the sheet surface of the AHSS as well as the interface between both sheet materials. The fundamental mechanism of this embrittlement phenomenon and the associated cracking in welds is not well understood, but cracking is believed to be due to the simultaneous effect of stress, high temperatures and the presence of a liquid metal (from the Zn-coated steel partner, or from the Cu-electrodes in RSW) during the spot-welding process. The liquid metal is believed to penetrate the grain boundaries of the steel, and lead to embrittlement and intergranular cracking. It has been shown, that a high welding current and a misalignment of the welding electrodes contribute to cracking in dissimilar spot welding. The cracks usually occur along grain boundaries in the HAZ of the AHSS. Due to the small scale of the cracks, there are challenges in terms of sample preparation and metallographic evaluation. Cross sectioning of spot welds can only capture a 2D

image of the HAZ around the weld nugget and might not expose cracking which occurs in the welds. At the same time non-destructive testing methods are usually not able to image these cracks due their small size. This might be one reason why the literature does not provide a lot of information about susceptible microstructures. Most of the current research concentrates on how to design a spot-welding process (weld schedule), so the cracking does not occur. While this is certainly important, an “assured” resistance of AHSS to LME cracking can only be achieved if the underlying causes of this type of cracking are revealed.

This research was conducted to assist in the understanding of the mechanism behind LME cracking. The first step in this process was reproducing LME cracking in the laboratory environment. Once cracking was obtained, metallurgical characterization and examination was conducted using LOM and SEM to help identify LME characteristics.

CHAPTER 2. BACKGROUND

2.1 Automotive Regulations

In 2012, the Department of Transportation (DoT) released in conjunction with the Environmental Protection Agency (EPA) future standards for fuel efficiency of domestically manufactured vehicles through the year 2025 (Table 1) [1]. To comply with these standards, automotive manufactures have taken three approaches (1) reducing the vehicles weight, (2) increasing efficiency of the powertrain, and (3) improving the aerodynamics of the vehicles. In order to use less material to achieve a body-in-white (vehicle skeleton) weight reduction, automotive manufacturers are using materials that are higher strength to comply with increasing safety standards.

Table 1: Minimum standard for domestically manufactured passenger cars (MPG).

Year	**2017**	**2018**	**2019**	**2020**	**2021**	**2022**	**2023**	**2024**	**2025**
MPG	36.7	38.0	39.4	40.9	42.7	44.7	46.8	49.0	51.3

2.2 Development of Advanced High-Strength Steels

Some of these steels being used by the automotive industry are known as Advanced High Strength Steels (AHSS) and were first developed in the late 1990's. AHSS are steels classified by their extremely high strengths, with tensile strengths exceeding 780 MPa [2]. Several types of AHSS have been developed including but not limited to Dual Phase (DP) Steels, Transformation Induced Plasticity (TRIP), Twinning-Induced Plasticity (TWIP), and Press-Hardened Boron Steels (PHBS). These steels are typically named for their complex microstructures or methods used to

attain their high strengths. While these steels are very high in strength, it typically comes at a cost to ductility as shown in Figure 1.

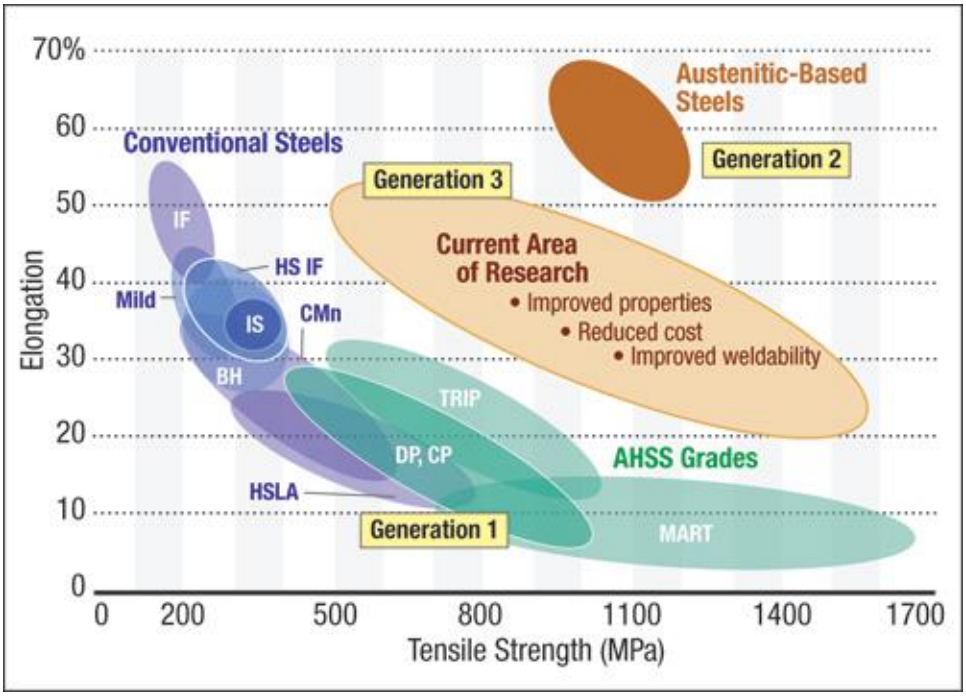

Figure 1: Graph of elongation vs. tensile strength for steels [3].

2.3 Dual Phase Steels

DP steels are named as such for the dual nature of their microstructure consisting of a softer ferrite (δ) and a hard martensite phase. Number designations (e.g. DP590) in the name for DP steels refer to the tensile strength of the specific steel. As the amount of martensite in the δ matrix increases, the material experiences an increase in strength and a reduction in ductility. DP steels are one of the most widely used AHSS in automotive applications and are used in different capacities dependent on strength. Lower strength DP steels such as DP590 are used in floor panels and outer door panels, while higher strength alloys such as DP980 are utilized in safety components such as B-pillars and engine cradles [4].

2.4 Press-Hardened Boron Steels

PHBS are also known as simply Boron (B) steels because of their utilization of B (0.002-0.005 %) to increase the hardenability of the material. PHBS are cut and blanked at room temperature (1), heated to the austenitic microstructure where they are stamped formed into their final part (2), and cooled rapidly to form martensite and achieve their final hardness (3) (Figure 2). PHBS tensile strengths can exceed 1500 MPa but the martensitic microstructure exhibits a low ductility. These steels are utilized highly in safety components of vehicles including A and B-pillars as well as cross members.

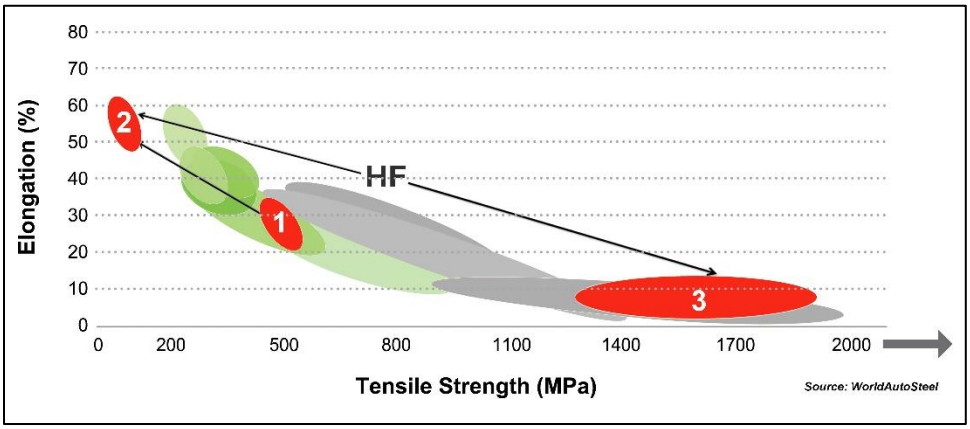

Figure 2: Heating cycle and mechanical properties of PHBS [5].

2.5 Utilization in Automotive

AHSS are being utilized in the different frame components dependent on strength and ductility requirements for safety purposes while achieving weight reductions. Figure 3 below shows an example of where these materials are being utilized in an automotive frame and an approximation of their body structure masses. In the rest of the vehicle, traditional lower strength low alloy steels are still being used, and in many cases these steels are being welding to the AHSS

using a combination of welding processes such as Resistance Spot Welding (RSW), Gas Tungsten Arc Welding (GTAW), and Gas Metal Arc Welding (GMAW). There are as many as 4500 RSW in a single vehicle.

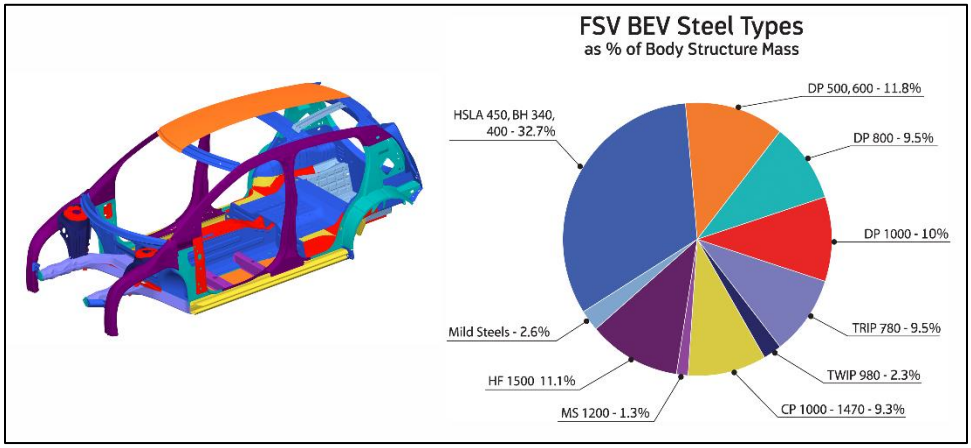

Figure 3: Example of locations and amounts of AHSS in an automotive frame [6].

2.6 Resistance Spot Welding

RSW utilizes a combination of force and the concept of Joule Heating to create a weld between two thin sheets of material. In equation 1 J=joule heating, I=current, R=resistance, and t=time. Note that current dominates this equation as its value is squared. In equation 2 for resistance ρ=resistivity of the material, l=current path length, and A=cross sectional area of the electrode to work piece contact [7]. A schematic representation of a typical RSW setup is displayed below in Figure 4 showing both electrodes, the work pieces, and the formation of the weld known as a weld nugget.

1 $J = I^2Rt$

2 $R = \frac{\rho l}{A}$

RSW uses highly conductive copper electrodes to pass the current through the work pieces which are of a less conductive material. The resistance through the electrodes and the work pieces are known as “bulk” resistance. Additionally, there is a resistance experienced at the interfaces both between the electrodes and the work pieces, and the two work pieces themselves. The highest resistance is located at the interface between the two work pieces, and this is where most of the heat is created by the current, and this is where the weld nugget is formed. Figure 4 shows a graphical representation of the relative resistances and the temperatures generated in a RSW.

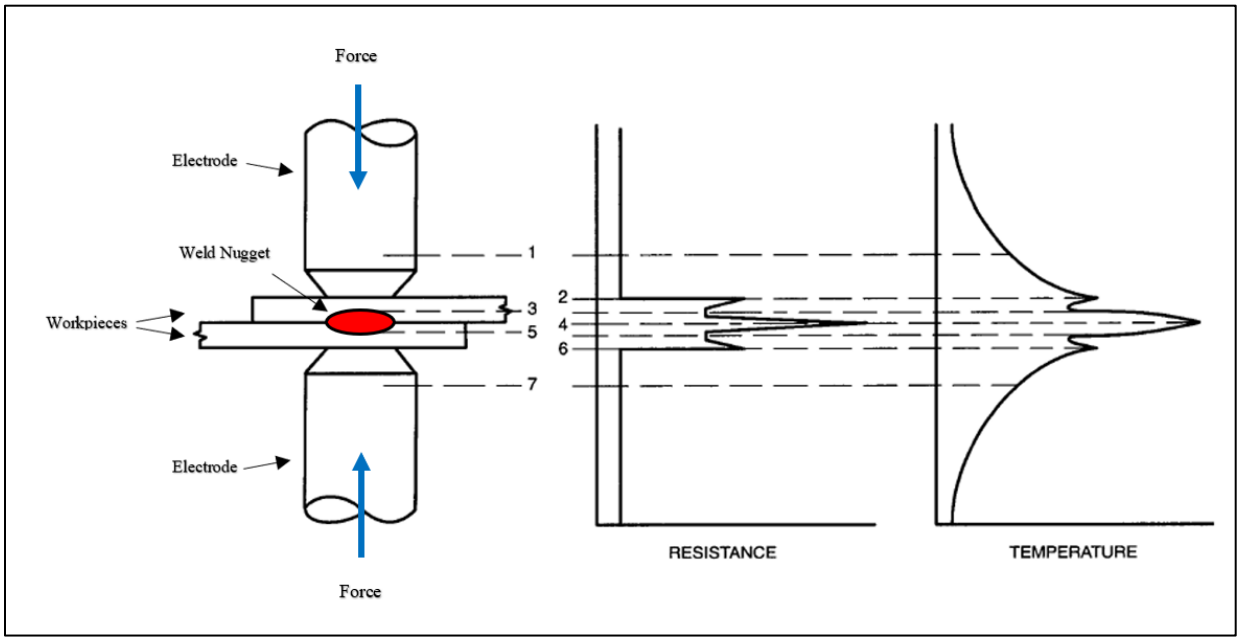

Figure 4: Schematic of RSW weld setup and graphs of resistance and temperature.

2.7 Liquid Metal Embrittlement

LME is described as the loss of ductility of an otherwise ductile metallic material in the presence of another liquid metal with lower melting temperature [8]. While LME cracking phenomenon has been studied for close to fifty years, the mechanism behind its occurrence is still not well understood. What has been accepted is that for LME to occur, three conditions need to be satisfied (Figure 5): **1)** a susceptible microstructure **2)** tensile stresses, and **3)** the presences of a metal with a lower melting temperature than the base material [9].

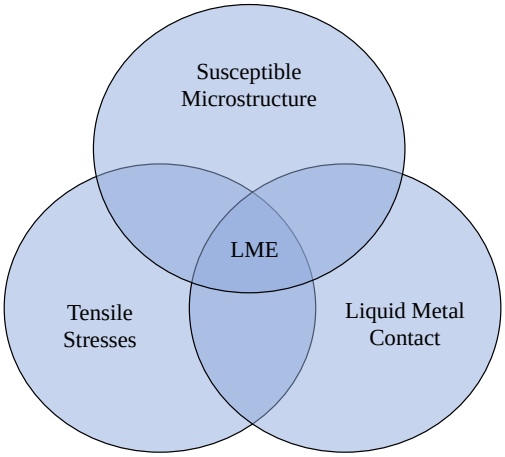

Figure 5: LME Venn diagram showing necessary conditions for cracking.

It is generally accepted that austenitic microstructures are more susceptible to LME cracking [10]. This is typically attributed to the early liquefaction of the Zn in the galvanizing material while at temperatures where the steel is in the austenite phase field [11]. It has also been suggested that the austenitic phase which experiences a higher coefficient of thermal expansion leads to higher thermal stresses during the weld cycle and may contribute to the onset of LME [12]. While austenitic microstructures may be more susceptible to LME cracking, there has been work that does suggest that with high enough strain rates (force) and temperatures (weld heating), LME

cracking will occur in completely ferritic, ferrite + martensite, martensitic microstructures [12] (see Figure 6).

	Strain rate (s^{-1})	600 °C	700 °C	800 °C	900 °C
DQ	1			LME	LME
	0.1			LME	LME
	0.01			LME	LME
DP	1	LME	LME	LME	LME
	0.1		LME	LME	LME
	0.01			LME	LME
TWIP	1		LME	LME	LME
	0.1		LME	LME	LME
	0.01			LME	LME

Figure 6: Results from Geunsu Jung et al.: LME occurrence in automotive steels with austenite (blue) and ferrite (orange) microstructure [12].

LME is most often observed as an intergranular cracking phenomenon (Figure 7) and suggests that grain size or structure may play a role [13]. The region of the HAZ adjacent to the FZ is considered the high temperature HAZ, and experiences grain growth (Figure 8). These larger grains may be easier to form LME cracks due to less grain boundary obstruction [14]. The embrittling phases are suspected to penetrate along the grain boundaries and lead to a loss in ductility leading to LME cracking [15].

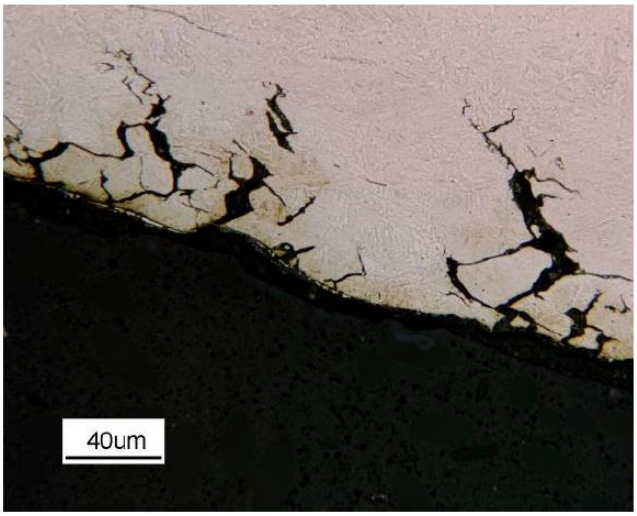

Figure 7: Intergranular LME cracking from Sigler et al. [16].

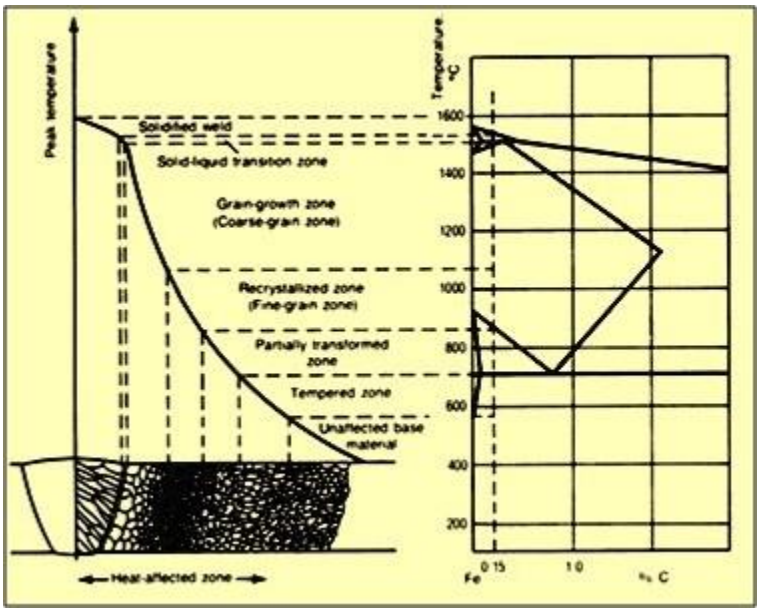

Figure 8: Fe-C phase diagram and associated weld regions.

There are two suggestions for the embrittling agent associated with LME that occurs with the Zn steel couple. The first being that the Zn melts at a lower temperature, and wets along the steel grain boundaries leading to a loss in ductility [13]. A second logic suggests that the formation of a Fe-Zn layer may occur, which has a higher melting temperature than pure Zn. Due to this, the

Fe-Zn would be retained and available at higher temperatures during the weld cycle when LME may occur [16]. There is also some suggestion that there is a reduction of mechanical properties in the base material due to the diffusion of Zn laterally into the prior austenitic grain boundaries instead of the presence of liquid Zn [12] (see Figure 9).

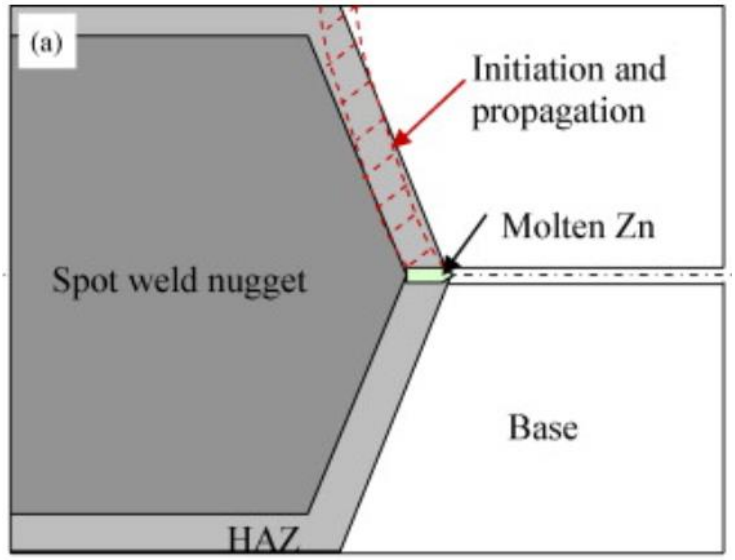

Figure 9: Schematic of Zn penetration and diffusion from Ma, C. et al. [19].

Tensile stresses are also a critical contributing factor for the occurrence of LME cracking. Experiments have been conducted to determine critical strain rates in Gleeble simulations [10, 17] as well as applying varying tensile forces during the RSW process [18]. Additionally, there has been evidence that LME cracking can lead to failure during service for Zn-coated AHSS [14]. With the lower melting temperature of Zn in conjunction with thermal/mechanical stresses during service can lead to Zn-penetration through the materials. Regarding mechanical properties, it is generally recognized that stronger steels are more susceptible to LME cracking [12]. This also agrees with LME occurring in the HAZ of the weld, where a significant increase in material

hardness is observed by typical microhardness profile due to martensitic transformation of this part of the HAZ [19].

There have also been suggestions that the formation of Al_2O_3 due to Al in the galvanization material may contribute to LME cracking. This oxide forms on the surface and may act as an insulator during the welding process [11]. This increases the current density during welding, and in turn increases the heating experienced by the material, and significantly increases the probability of surface cracking. The Usibor-1500 material is coated with Al-Si to offer some corrosion resistance during the forming process and may provide the Al necessary to experience this effect [20]. These coatings may also significantly affect RSW welding parameters and joint properties [21].

Cooling rate is one more factor that may induce LME that is investigated during these experiments. Effects of using an ice spray (-40 °C) was used to cool the top plate to simulate extreme welding conditions in a study performed by Rethmeier [18]. The use of Class-II Type-B domed electrodes have been suggested to provide non-uniform cooling and lead to different stresses during the cooling of the materials post weld [22]. Some suggest that dome shaped electrodes may also lead to weld nugget geometry formations that may affect LME [23].

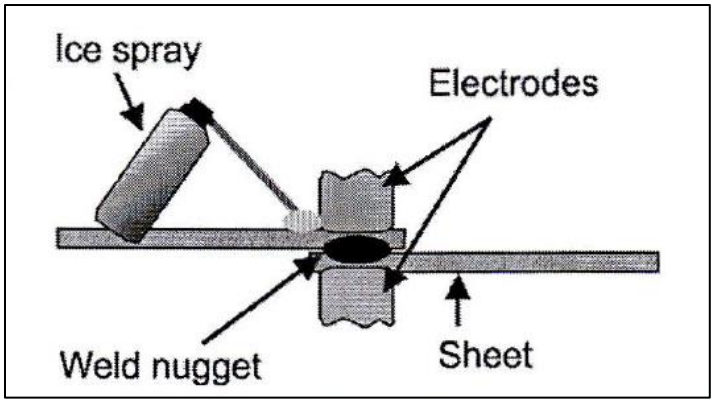

Figure 10: Application of ice spray as used in LME study by Gaut et al. [18].

CHAPTER 3. OBJECTIVES

This undergraduate research project was conducted to support further work investigating the fundamental mechanisms behind LME. The specific objectives of this project are as follows.

1. **Literature Review –** review of current literature on LME cracking, specifically in cases with AHSS and dissimilar RSW combinations with Zn-coated steel grades.

2. **LME Crack Reproduction -** reproduce LME induced cracking in dissimilar RSW in a laboratory environment by varying welding parameters, and the introduction of additional restraint during welding

3. **Crack Characterization -** develop metallographic procedures to examine the cracking, and characterize the LME crack location and morphology

CHAPTER 4. EXPERIMENTAL PROCEDURE

4.1 Materials

Four test materials were used in this project including three AHSS (DP590, DP980, and Usibor-1500) and one Zn-galvanized plain carbon steel. Their chemical compositions are listed in Table 2. The base metals were examined to determine microstructures and phase volume fractions. The Zn-galvanized plain carbon steel was a combination of ferrite and the pearlite micro constituent. The two DP steels, DP590 and DP980, microstructures were comprised of ferrite and martensite phases. Lastly the PHBS, Usibor-1500, was completely martensitic in composition. Using ImageJ software to determine the phase volume fractions of the two DP steels, the DP590 was approximately 28% martensite and 72% ferrite. The phase volume fraction of the DP980 steel was approximately 54% martensite and 46% ferrite. The mechanical properties are also documented below in Table 3.

Table 2: Experimental Materials Composition and Thickness (Source: Arcelor-Mittal)

Material	**C_{max}**	**Mn_{max}**	**Si_{max}**	**B_{max}**	**Fe**	**Thickness**
DP590	0.1	1	0.3	–	Balance	1.4
DP980	0.15	1.4	0.3	–	Balance	1.4
Usibor-1500	0.25	1.4	0.4	0.005	Balance	1.5

Table 3: Experimental Materials Mechanical Properties (Source: Arcelor-Mittal)

Material	**Yield Strength (MPa)**	**Tensile Strength (MPa)**	**Ductility (% Elongation)**
DP590	400	630	27
DP980	600	1030	13.8
Usibor-1500	1100	1500	≥3

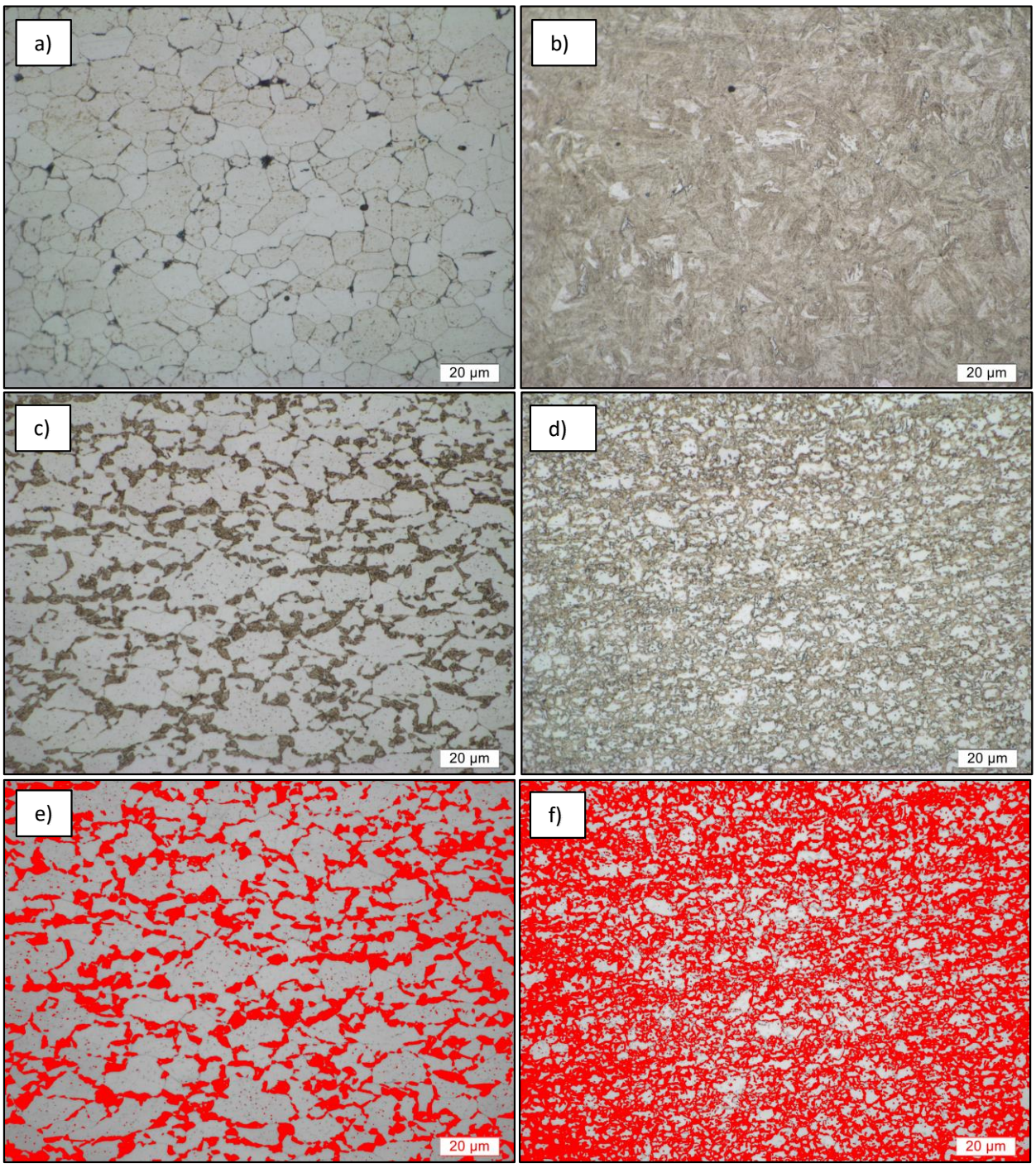

Figure 11: Microstructures of experimental materials a) plain carbon steel b) Usibor-1500 c) DP590 d) DP980 etched with 2% nital, and phase fraction analysis of Dual Phase steels e) DP590 and f) DP 980

4.2 Welding Equipment

Two different welding machines were used during experimentation. The first being a Taylor-Winfield pneumatic AC (Alternating Current) pedal stool type welder, operating at a maximum of 34 kA. This system used a MEDWELD 3000s AC welding controller and a Pertron Model CIR 1000 DC (Direct Current) Weld-Checker. This welder was utilized for weld sets #1 - #3. This machine provided less control over both force and current.

The second machine was an Obara MFDC (Medium Frequency Direct Current) Model # U1-016965 servo driven pedal stool type welder, operating at a maximum of 65 kA. This system ran with a Welding Technology Corp. WT6000 MFDC welding Control. This weld system offered complete control over both current and force, and was used for Weld Sets #2 - #17.

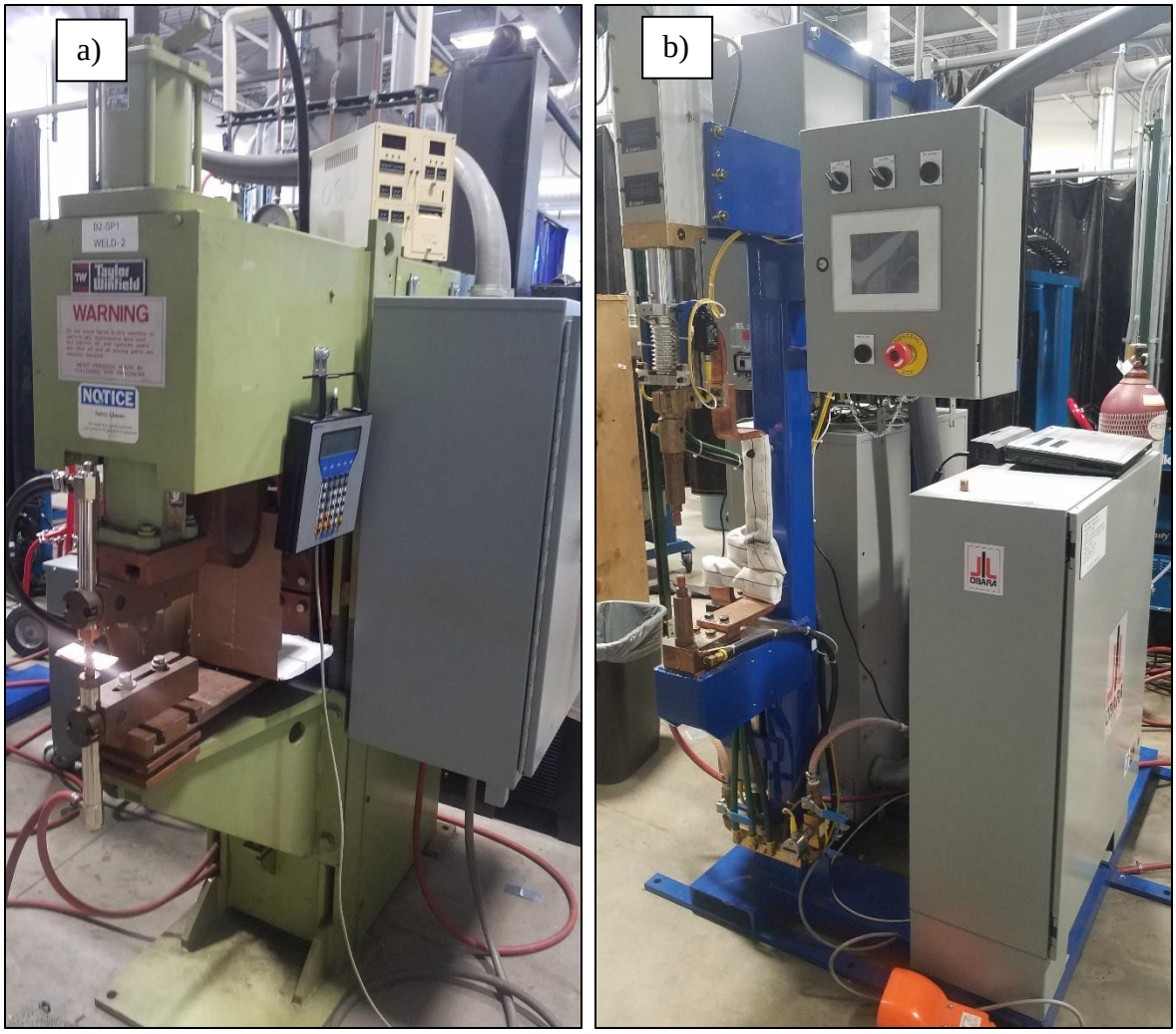

Figure 12: RSW machines a) pneumatic AC RSW b) MFDC RSW

4.3 Welding Procedures

4.3.1 Pneumatic Resistance Welder – Weld Sets #1 - #3

Weld sets #1 - #3 were performed on the Taylor-Winfield AC RSW using constant weld parameters of Type-E Class II (alloy of Cr and Cu) electrodes with a face diameter of 6.75 mm, weld time of 13 cycles, and hold time of 60 cycles (Table 4). One weld was performed on each AHSS in combination the Zn-galvanized steel for each weld set. These initial weld parameters

were chosen based off recommended practices from AWS C1.1. This type of RSW did not allow for specific current to be programed, but rather the use of a transformer tap setting and heat percentage. The tap setting controlled the peak of the AC wave function, and the heat percentage the amount of the wave formed utilized during welding. Optimal settings utilize lowest tap setting and maximum heat percentage to capitalize on using most of the power generated for efficiency. Weld times were programed in cycles (1 cycle = 0.0167 sec.).

Table 4: Weld Sets #1-#3 Using a Pneumatic Resistance Welder

Material Resistance Welded to Galvanized Steel				**11/2/2017**	**Weld Set #1**	**Pneumatic Resistance Welder**		
Material	**Electrode Shape**	**Face Diameter (mm)**	**Force (lbs)**	**Weld Cycles**	**Hold Cycles**	**Current (kA)**	**Tap Setting**	**HT %**
DP590	Type-E	6.75	700	13	60	8.5	Low 2	60
DP980	Type-E	6.75	700	13	60	8.4	Low 2	60
Usibor	Type-E	6.75	700	13	60	8.7	Low 2	60
Material Resistance Welded to Galvanized Steel				**11/2/2017**	**Weld Set #2**	**Pneumatic Resistance Welder**		
Material	**Electrode Shape**	**Face Diameter (mm)**	**Force (lbs)**	**Weld Cycles**	**Hold Cycles**	**Current (kA)**	**Tap Setting**	**HT %**
DP590	Type-E	6.75	600	13	60	8.8	Low 3	70
DP980	Type-E	6.75	600	13	60	8.3	Low 3	70
Usibor	Type-E	6.75	600	13	60	8.8	Low 3	70
Material Resistance Welded to Galvanized Steel				**11/2/2017**	**Weld Set #3**	**Pneumatic Resistance Welder**		
Material	**Electrode Shape**	**Face Diameter (mm)**	**Force (lbs)**	**Weld Cycles**	**Hold Cycles**	**Current (kA)**	**Tap Setting**	**HT %**
DP590	Type-E	6.75	700	13	60	8.5	Low 3	70
DP980	Type-E	6.75	700	13	60	12.0	Low 3	90
Usibor	Type-E	6.75	700	13	60	12.2	Low 3	90

4.3.2 3-D Printed Fixture – Weld Set #4

Weld Set #4 utilized the MFDC RSW and the use of a 3-D printed fixture to apply additional tensile stresses to the AHSS during the welding process. The designs were constructed in SolidWorks CAD programing, and printed using a Creality CR-10 printer and a PLA polymer. (Figure 13). A schematic of the 3-D model with specific dimensions is in appendix A. Two iterations of the fixture were produced, the first as a test production at a lower density to gain

insight as to how the design would perform. The second at a higher density for added strength, and with slight modifications in design primarily increasing the material separation to 4.5 mm (Figure 15).

One weld was performed for each AHSS in dissimilar metal combination with the Zn-galvanized steel for Weld Set #4. While the fixture was able to deform the two DP steels prior to performing the weld sequence, the polymer material strength was not enough to deform the Usibor-1500 before the fixture fractured. It was noted that the fixture was required to be cut into two pieces to allow for the removal of the steel samples once the welding process was complete (Figure 14). It has been suggested that forces provided during the welding process alone are not enough to cause LME [8]. So higher forces of 900 lbs were used for this weld set to provide the necessary contact of the separated materials to be welded, providing additional stresses. Deforming the sheets was suggested by Gaul et al as a possible cause of LME cracking [18]. Additional weld parameters used were Type-E Class II electrodes, weld time of 267 msec, hold time of 300 msec, and current of 12 kA (Table 5). Higher currents were utilized from Weld Sets #1 - #3 to provide more heat input in addition to the higher stresses. After welding, the weld samples of the two DP steels were examined for surface cracking before metallographic preparation.

Table 5: Weld Set #4 Using 3-D Printed Jig

Material Resistance Welded to Galvanized Steel				**11/2/2017**	**Weld Set #4**	**3-D Printed Jig**		
Material	**Electrode Shape**	**Face Diameter (mm)**	**Force (lbs)**	**Weld Time (msec)**	**Hold Time (msec)**	**Current (kA)**	**Tap Setting**	**HT %**
DP590	Type-E	6.75	900	267	300	12	–	–
DP980	Type-E	6.75	900	267	300	12	–	–
Usibor	Type-E	6.75	900	–	–	–	–	–

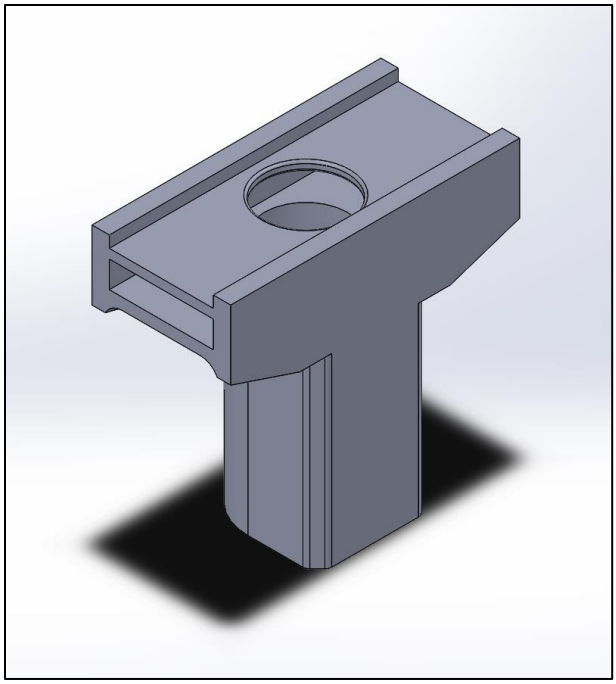

Figure 13: SolidWorks 3-D model of RSW fixture.

Figure 14: 3-D printed job utilized during Weld Set # 4

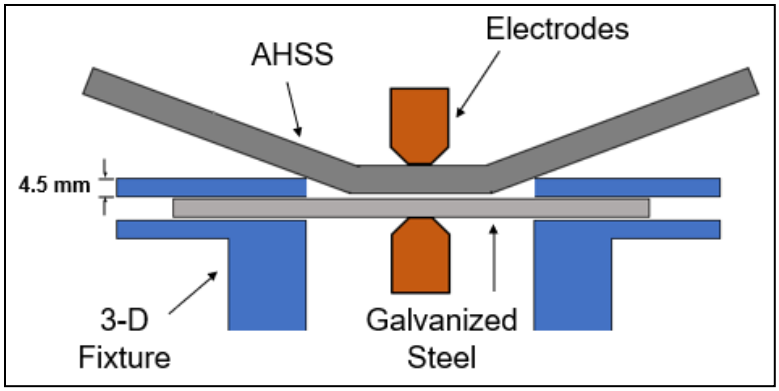

Figure 15: Schematic of weld setup utilized during Weld Set #4

4.3.3 Modified Type-E Electrode – Weld Sets #5 and #14 - #17

Weld Set #5 and Sets #14 - #17 utilized two sets of modified electrodes designed to provide an offset and additional stresses in the materials while being welded. Electrode misalignment was suggested by Gaul et al as another possible source causing LME cracking [18]. The first set was not standardized and was machined using a bench grinder (Figure 16), which provided for a rough and uneven surface finish. Lower forces were used in weld Set #5 than in Set #4, as the increased forces were not required to overcome sheet separation. The rest of the weld parameters were held constant from weld Set #4 (Table 6).

One weld was performed on each AHSS in dissimilar combination with the Zn-galvanized steel. These offset electrodes were designed to impose additional stresses in a different plane than the typical compressive forces provided by a RSW process (Figure 17). These samples were inspected for surface cracking both optically and using dye penetrant testing spray. After surface

inspection, the samples were metallographically prepared for LOM examination. These samples were further prepared for SEM examination.

Table 6: Weld Set #5 Using Modified Electrode #1

Material Resistance Welded to Galvanized Steel				11/2/2017	Weld Set #5	Modified Electrode #1		
Material	**Electrode Shape**	**Face Diameter (mm)**	**Force (lbs)**	**Weld Time (msec)**	**Hold Time (msec)**	**Current (kA)**	**Tap Setting**	**HT %**
DP590	Type-E	I	700	267	300	12	I	I
DP980	Type-E	I	700	267	300	12	I	I
Usibor	Type-E	I	700	267	300	12	I	I

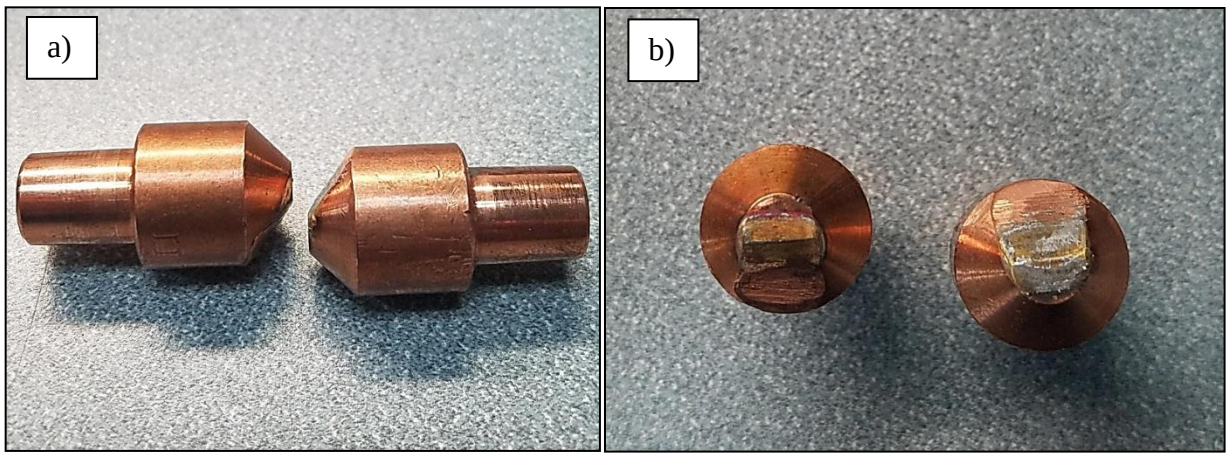

Figure 16: Modified electrodes Set #1 a) side view b) top view

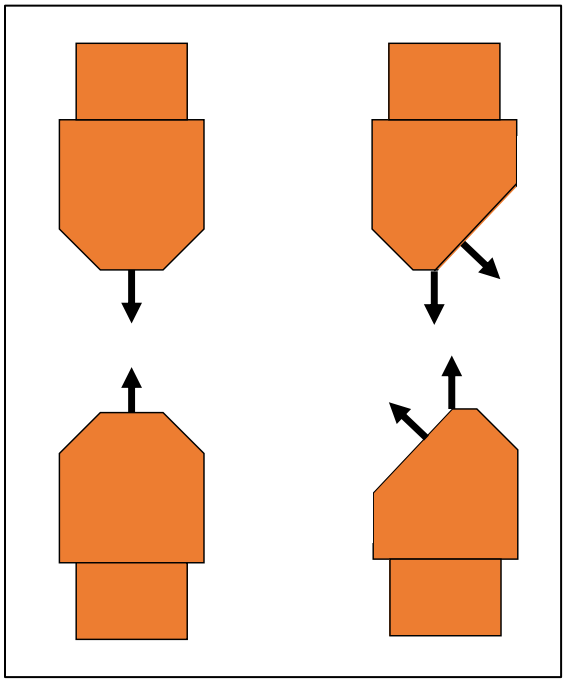

Figure 17: Schematic of force directions from modified electrodes.

Due to the success of obtaining interfacial cracking from Weld Set #5, a second set of electrodes were designed using a systematic material removal process. Electrode shapes were designed using SolidWorks CAD software (and drawn on to electrodes to provide guidelines while machining. The second set of modified electrodes were more uniform in design with substantially

better surface finishes. Weld Sets #14 - #17 were performed using combinations of high force – low current, high force – high current, low force – low current, and low force – high current. Weld and hold times were held constant for Set #14 - #17 (Table 7). One weld was performed on each AHSS in dissimilar combination with the Zn-galvanized steel. Additionally, for Weld Set #14, the Al-Si coating was removed from the Usibor-1500 material. The sample was then electro-galvanized using a $ZnSO_4$ solution and parameters of 6 volts, 1 amp, and a time of 10 minutes. This was done achieve two goals **1)** remove the Al-Si coating to see if it was affecting LME and **2)** provide additional Zn at both the interface and surface of the material during welding. After welding, the samples were inspected for surface cracking before metallographic preparation for LOM examination.

Table 7: Weld Sets #14 - #17 Using Modified Electrode #2

Material Resistance Welded to Galvanized Steel				**11/2/2017**	**Weld Set #14**	**Modified Electrode #2**		
Material	**Electrode Shape**	**Face Diameter (mm)**	**Force (lbs)**	**Weld Time (msec)**	**Hold Time (msec)**	**Current (kA)**	**Tap Setting**	**HT %**
DP590	Type-E	⊢	800	300	167	12	⊢	⊢
DP980	Type-E	⊢	800	300	167	12	⊢	⊢
Usibor	Type-E	⊢	800	300	167	12	⊢	⊢
Material Resistance Welded to Galvanized Steel				**11/2/2017**	**Weld Set #15**	**Modified Electrode #2**		
Material	**Electrode Shape**	**Face Diameter (mm)**	**Force (lbs)**	**Weld Time (msec)**	**Hold Time (msec)**	**Current (kA)**	**Tap Setting**	**HT %**
DP590	Type-E	⊢	800	300	167	14	⊢	⊢
DP980	Type-E	⊢	800	300	167	14	⊢	⊢
Usibor	Type-E	⊢	800	300	167	14	⊢	⊢
Material Resistance Welded to Galvanized Steel				**11/2/2017**	**Weld Set #16**	**Modified Electrode #2**		
Material	**Electrode Shape**	**Face Diameter (mm)**	**Force (lbs)**	**Weld Time (ms)**	**Hold Time (msec)**	**Current (kA)**	**Tap Setting**	**HT %**
DP590	Type-E	⊢	500	300	167	12	⊢	⊢
DP980	Type-E	⊢	500	300	167	12	⊢	⊢
Usibor	Type-E	⊢	500	300	167	12	⊢	⊢
Material Resistance Welded to Galvanized Steel				**11/2/2017**	**Weld Set #17**	**Modified Electrode #2**		
Material	**Electrode Shape**	**Face Diameter (mm)**	**Force (lbs)**	**Weld Time (msec)**	**Hold Time (msec)**	**Current (kA)**	**Tap Setting**	**HT %**
DP590	Type-E	⊢	500	300	167	14	⊢	⊢
DP980	Type-E	⊢	500	300	167	14	⊢	⊢
Usibor	Type-E	⊢	500	300	167	14	⊢	⊢

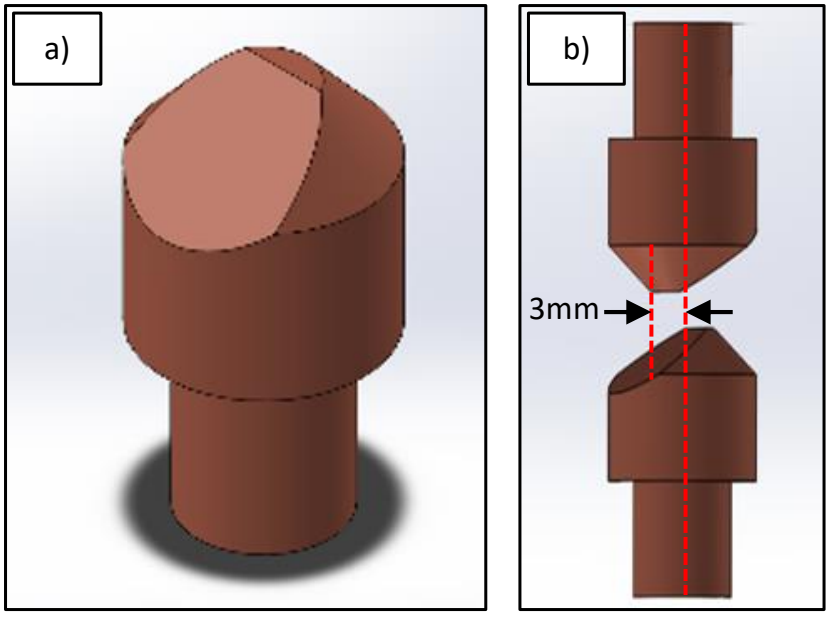

Figure 18: 3-D model of modified electrode set #2

Figure 19: Modified Electrode Set #2.

4.3.4 Liquid Nitrogen Cooling – Weld Set #6

Weld Set #6 was performed using a high weld force, shorter weld time, and lower weld current (Table 8). An ice spray that was used during Gaul et al study was not available [18], so the samples were all cooled by total emersion into liquid Nitrogen before welding. One weld was performed on each AHSS in dissimilar metal combination with the Zn-galvanized steel for each weld set. These samples were inspected for surface cracking post weld using dye penetrant testing spray. Afterwards, the samples were metallographically prepared for LOM examination.

Table 8: Weld Set #6 Using Liquid N

Material Resistance Welded to Galvanized Steel				**11/2/2017**	**Weld Set #6**	**Liquid N Cooled**		
Material	**Electrode Shape**	**Face Diameter (mm)**	**Force (lbs)**	**Weld Time (msec)**	**Hold Time (msec)**	**Current (kA)**	**Tap Setting**	**HT %**
DP590	Type-E	6.75	900	200	300	10	–	–
DP980	Type-E	6.75	900	200	300	10	–	–
Usibor	Type-E	6.75	900	200	300	10	–	–

4.3.5 3-Stack Weld Set Up – Weld Set #7

Weld Set #7 was made attempting to place Zn at two interfaces by utilizing a three-stack set up placing the Zn-Galvanized steel between two samples of AHSS (Figure 20). Weld Set #7 also attempted to apply addition stresses on the materials by using the 3-D printed fixture used during Weld Set #4 (Figure 21). Higher forces were used to compress the three-stack setup, a lower current, and an extremely low hold time (Table 9). One weld was performed for each AHSS in dissimilar metal combination with the Zn-galvanized steel for this weld set. A successful weld was not made on the Usibor-1500 material. The samples from the two DP Steels were examined for surface cracking before metallographic preparation and LOM examination.

Table 9: Weld Set #7 Using 3 Stack Weld Setup

Material Resistance Welded to Galvanized Steel				11/2/2017	Weld Set #7	3-Layer Setup		
Material	**Electrode Shape**	**Face Diameter (mm)**	**Force (lbs)**	**Weld Cycles**	**Hold Cycles**	**Current (kA)**	**Tap Setting**	**HT %**
DP590	Type-E	6.75	950	200	5	8	⊢	⊢
DP980	Type-E	6.75	950	200	5	8	⊢	⊢
Usibor	Type-E	6.75	950	⊢	⊢	⊢	⊢	⊢

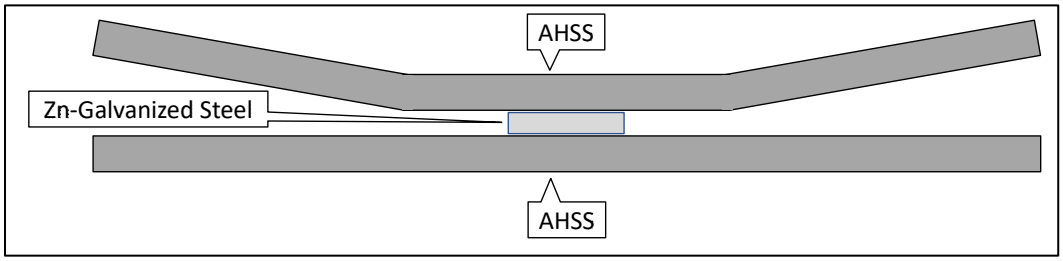

Figure 20: Schematic of three-stack set-up from Weld Set #7.

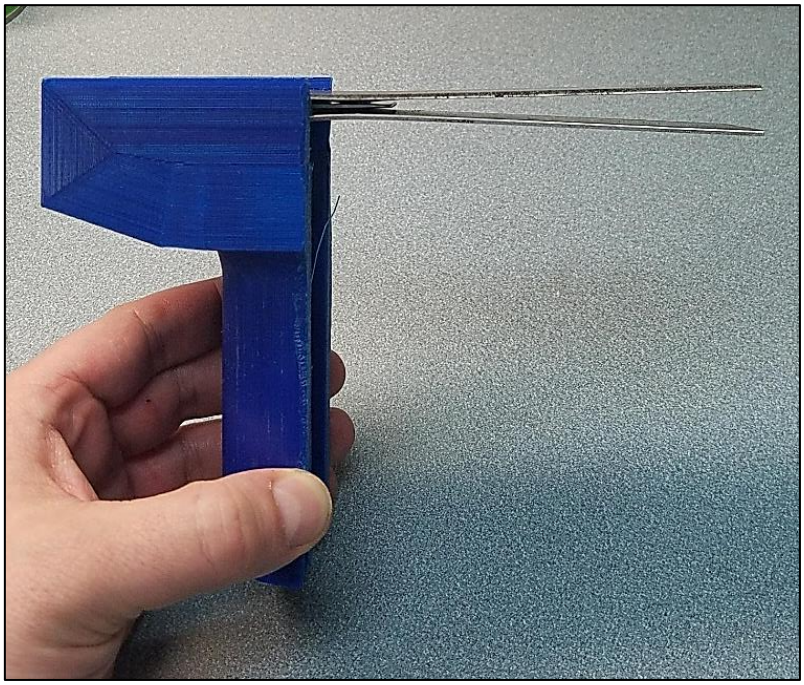

Figure 21: Three stack weld setup utilized during Weld Set #7

4.3.6 Class II Type-B Domed Electrode – Weld Sets #8 - #10

Weld Set #8 - #10 were performed utilizing a Type -B domed electrodes instead of the Type-E truncated electrodes, causing non-uniform cooling was suggested by Ashiri et al [23]. Forces used were varied between the sets, while utilizing a long weld time, short hold time, and low current (Table 10) as suggested by Kim et al [22]. One weld was performed on each AHSS in dissimilar combination with the Zn-galvanized steel. The welds were first inspected for surface cracking before metallographic preparation and LOM examination.

Table 10: Weld Sets #8 - #10 Using Class II Domed Electrode

Material Resistance Welded to Galvanized Steel				11/2/2017	Weld Set #8	Domed Electrode Class II		
Material	**Electrode Shape**	**Face Diameter (mm)**	**Force (lbs)**	**Weld Time (ms)**	**Hold Time**	**Current (kA)**	**Tap Setting**	**HT %**
DP590	Type-B	6.00	1000	400	50	7.5	–	–
DP980	Type-B	6.00	1000	400	50	7.5	–	–
Usibor	Type-B	6.00	1000	400	50	7.5	–	–
Material Resistance Welded to Galvanized Steel				**11/2/2017**	**Weld Set #9**	**Domed Electrode Class II**		
Material	**Electrode Shape**	**Face Diameter (mm)**	**Force (lbs)**	**Weld Time (ms)**	**Hold Cycles**	**Current (kA)**	**Tap Setting**	**HT %**
DP590	Type-B	6.00	800	400	50	7.5	–	–
DP980	Type-B	6.00	800	400	50	7.5	–	–
Usibor	Type-B	6.00	800	400	50	7.5	–	–
Material Resistance Welded to Galvanized Steel				**11/2/2017**	**Weld Set #10**	**Domed Electrode Class II**		
Material	**Electrode Shape**	**Face Diameter (mm)**	**Force (lbs)**	**Weld Time (ms)**	**Hold Cycles**	**Current (kA)**	**Tap Setting**	**HT %**
DP590	Type-B	6.00	900	400	50	7.5	–	–
DP980	Type-B	6.00	900	400	50	7.5	–	–
Usibor	Type-B	6.00	900	400	50	7.5	–	–

4.3.7 External Clamping System – Weld Sets #11 - #13

In order to apply a large amount of external tensile stresses to the AHSS materials while being welded, a clamping system as utilized, bending the steel samples over the bottom electrode (Figure 22). Type-B domed electrodes were used for all three weld sets. Different combinations of weld force and current were used, while weld and hold times were held constant (Table 11). One weld was performed on each AHSS in dissimilar combination with the Zn-galvanized steel for each weld set. The samples were inspected for surface cracking before metallographic preparation and LOM examination.

Table 11: Weld Sets #11 - #13 Using External Clamping System

Material Resistance Welded to Galvanized Steel				11/2/2017	Weld Set #11	External Clamping		
Material	**Electrode Shape**	**Face Diameter (mm)**	**Force (lbs)**	**Weld Time (ms)**	**Hold Cycles**	**Current (kA)**	**Tap Setting**	**HT %**
DP590	Type-B	6.00	700	267	167	12	I	I
DP980	Type-B	6.00	700	267	167	12	I	I
Usibor	Type-B	6.00	700	267	167	12	I	I
Material Resistance Welded to Galvanized Steel				**11/2/2017**	**Weld Set #12**	**External Clamping**		
Material	**Electrode Shape**	**Face Diameter (mm)**	**Force (lbs)**	**Weld Time (ms)**	**Hold Cycles**	**Current (kA)**	**Tap Setting**	**HT %**
DP590	Type-B	6.00	500	267	167	12	I	I
DP980	Type-B	6.00	500	267	167	12	I	I
Usibor	Type-B	6.00	500	267	167	12	I	I
Material Resistance Welded to Galvanized Steel				**11/2/2017**	**Weld Set #13**	**External Clamping**		
Material	**Electrode Shape**	**Face Diameter (mm)**	**Force (lbs)**	**Weld Time (ms)**	**Hold Cycles**	**Current (kA)**	**Tap Setting**	**HT %**
DP590	Type-B	6.00	700	267	167	9	I	I
DP980	Type-B	6.00	700	267	167	9	I	I
Usibor	Type-B	6.00	700	267	167	9	I	I

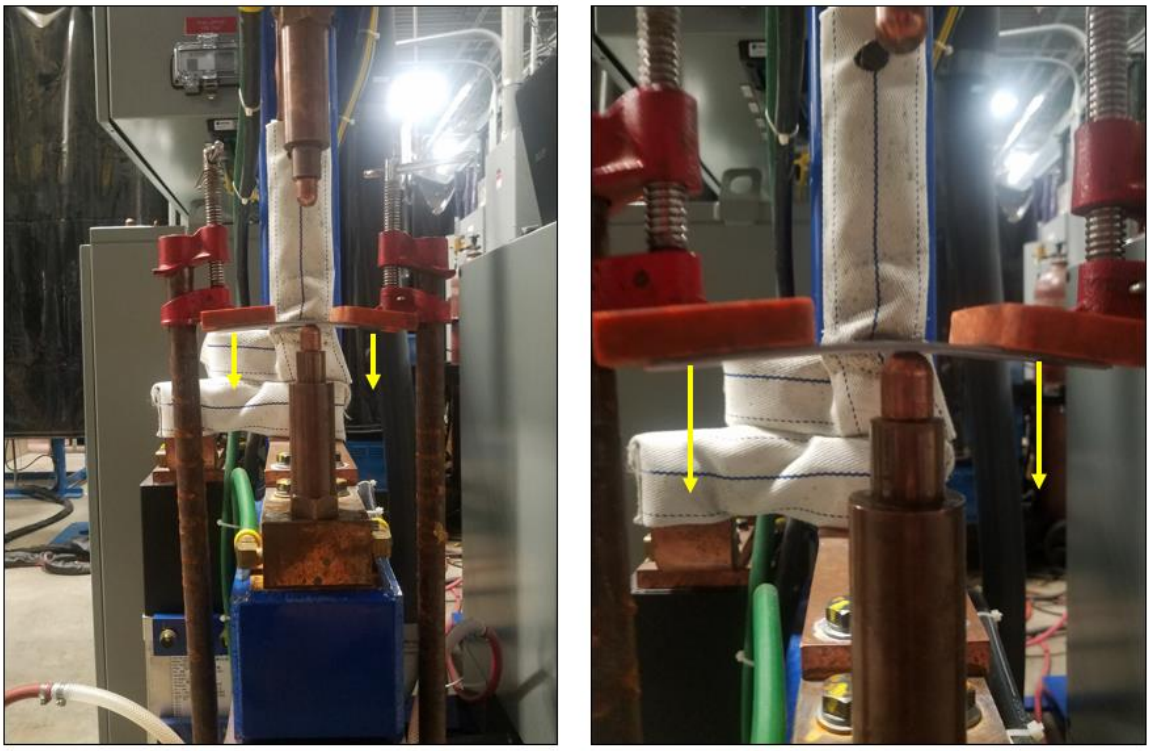

Figure 22: External clamping system utilized in Weld Sets #11 - #13.

4.4 Weld Examination Procedure

All samples were examined optically for surface cracking using a Nikon SMZ1000 camera. Samples from Weld Sets #5 and #6 were inspected for surface cracking using dye penetrant testing spray. Samples from Weld Sets All Samples were metallographically prepared for examination. Samples were first sectioned using an Allied High-Tech Productions Inc. TECHCUT 5 off center of the weld nugget (Figure 23). Samples from Weld Sets #1 - #3 were mounted in clear epoxy resin. The clear epoxy resin was initially used to allow for visual determination of where in the weld sample weld nugget was being inspected, a visualization of this is schematically represented in (Figure 24). The epoxy resin proved to lead to difficulty when polishing the samples, holding on to moisture and not allowing for the samples to dried completely. It was determined that these difficulties outweighed the benefits, and the epoxy mounting approach was abandoned for a traditional press mounting system in bakelight.

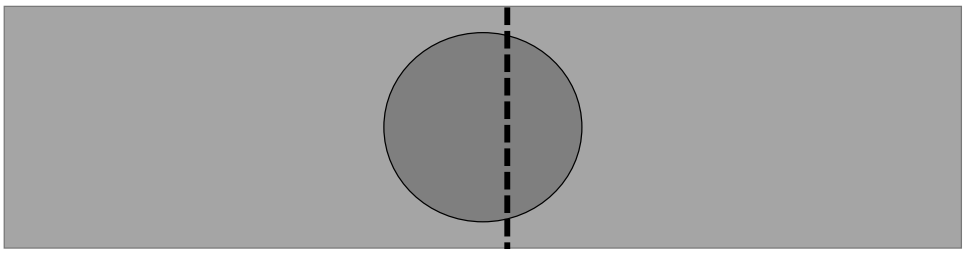

Figure 23: Schematic of sample cross-section approach.

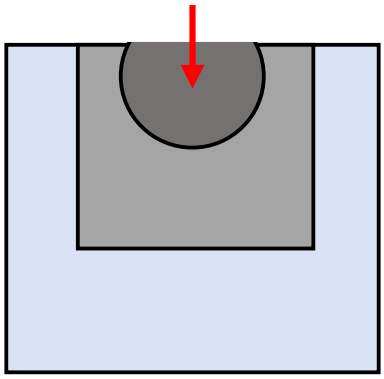

Figure 24: Schematic of epoxy resin mounting setup.

Samples from Weld Sets #4 - #10 were mounted in bakelight using a LECO PR-32 mounting press in 1.5” samples. Weld Sets #11 - #17 were mounted in conductive bakelight using a LECO PR-15 mounting press. Samples from Weld Sets # 4 - # 6 were inspected using dye penetrant testing, which did not reveal any surface cracking on any samples. All samples were first ground using a LECO BG-30 before a rough polish using 240, 320, 400, and 600 grit sand papers successively. Samples from Weld Sets #1 - #10 were polished using a Spectrum System 1000 polishing wheel using 6 μm and 1 μm diamond polishing paste sequentially. A Branson 2510 ultrasonic cleaner was used to clean samples between polishing. Samples from Weld Sets #11 - #17 were polished using a Pace Technologies Nano 1000T polishing wheel using 6 μm and 1μm diamond paste sequentially. All samples were inspected using Nikon Epiphot LOM. Samples where cracking was observed were taken for SEM inspection using FEI Apero microscope, using Backscattered Electrons (BSE) and Energy Dispersive X-Ray Spectroscopy (EDS) contrast detector.

CHAPTER 5. RESULTS AND DISCUSSION

5.1 Variation in Welding Force and Heat Input – Weld Sets #1 - #3

The first three weld sets were performed on the Taylor-Winfield pneumatic AC pedal stool RSW system. This machine offered no direct current control, and only approximate force control. The baseline for these welds were weld parameters suggested by AWS C1.1 for high strength steels. The welding force was varied between 600 and 700 lbs, and the heat input was varied between 60, 70 and 90% due to the given machine current control. No surface cracking in the AHSS was observed upon initial visual inspection of the welds using a stereomicroscope. Upon metallurgical preparation of the cross-sections (through the center of weld nugget) and examination using LOM, no evidence of cracking was observed in any of the AHSS.

5.2 Application of Addition Stresses During Welding Using a 3-D Printed Fixture – Weld Set # 4

The presence of tensile stresses is reported to be one of the requirements for LME cracking. In this work one of the approaches to induce cracking in the RSW joints was to apply additional stresses during welding using a 3D printed fixture. The fixture was designed to provide a physical separation between the AHSS and the Zn-galvanized steel. Increased welding forces (900 lbs) were used and applied by the RSW electrodes in order to deform the AHSS sheets so that a weld could be made. While the 3D printed fixture was strong enough to withstand the stresses created in order to deform the two dual phase steels, the high strength of the Usibor-1500 led to the fracture of the fixture. Nevertheless, a successful weld was made for all three dissimilar metal combinations, i.e. a weld nugget was formed in between the two sheets. Upon visual examination

of the weld surface and LOM evaluation of the cross-sections, no evidence of LME cracking was observed in any of the welds.

5.3 Application of Addition Stresses During Welding Using Modified E-Type Electrodes – Weld Sets #5 and #14 - #17

5.3.1 Modified Electrodes Set #1 - Weld Set #5

Another approach to introduce additional stresses during welding that was explored in this study to induce LME cracking was the use of an offset between the RSW electrodes. This was realized by modifying the geometry of the electrode face as described in section 4.3.3. The cross-sections of the welds made with electrode offset are shown in Figure 25. Successful welds with a formation of a weld nugget between both sheets were made for all AHSS. It is apparent though, that both the Zn-coated plain carbon steel and the AHSS sheets are highly deformed in the weld region. The electrode indentations are clearly visible on both sides. The weld nugget that formed is also highly deformed and non-symmetrical.

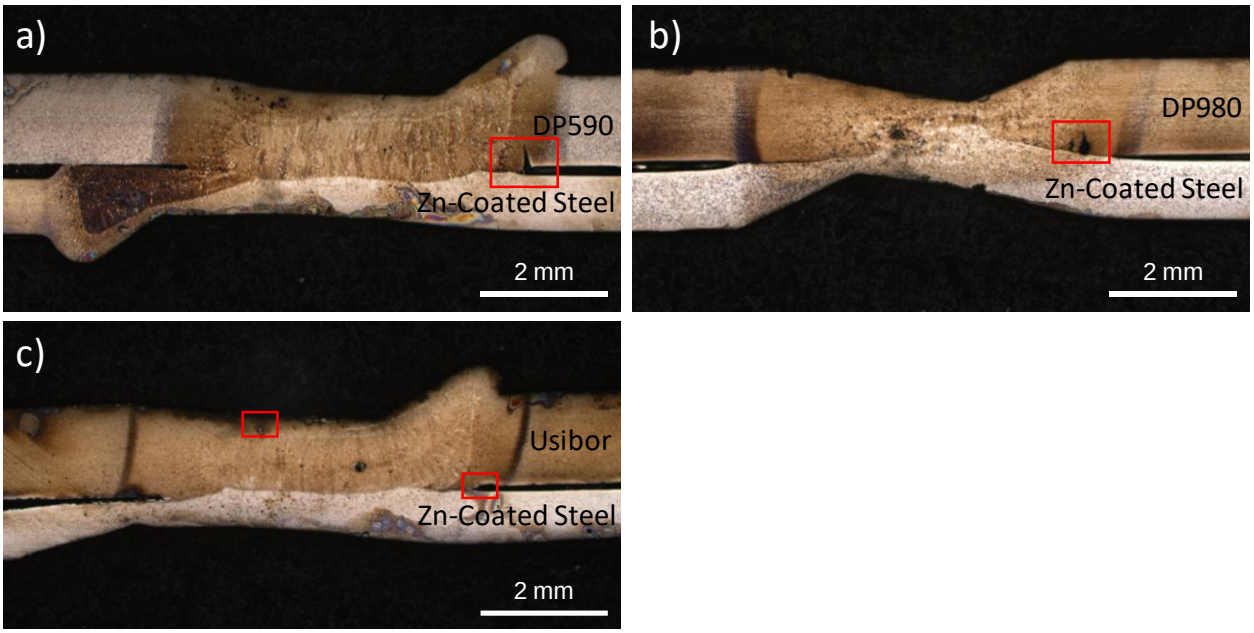

Figure 25: LOM micrographs (etched with 2% Nital) of weld cross-sections of weld set #5 samples: a) DP590, b) DP980, and c) Usibor-1500. Red rectangles mark the location of observed cracking in the weld cross-sections.

Several cracks were observed in the prepared cross-sections of these welds. The location of the observed cracks is marked in Figure 25 with red rectangles. In the welds on DP590 and DP980, cracks were observed in the HAZ of the AHSS in between the two steel sheets. No cracking was observed in the Zn-coated plain carbon steel. The cracks were about 500 µm and 300 µm away from the fusion line in the DP590 and DP980 weld, respectively. Characterization of the HAZ microstructure around the cracks indicates that they occurred in both dual phase steels in the fine-grained region of the HAZ. Details of the etched (2% Nital) HAZ microstructure surrounding the crack in the DP590 weld are shown in Figure 26. Figure 27 shows the cracking observed in the DP980 weld in the as-polished cross-section. In both cases, it can be seen that the crack opening is quite large, which indicates the high deformation in this region of the weld. In as-polished condition some branching of the cracking can be seen. The crack path is intergranular along prior austenite grain boundaries in the fine grained HAZ of the welds. This region of the HAZ was heated above the A_{c3} temperature during the weld thermal cycle and got fully transformed into

austenite. Upon cooling this austenite transformed into martensite due to the high cooling rates during resistance spot welding.

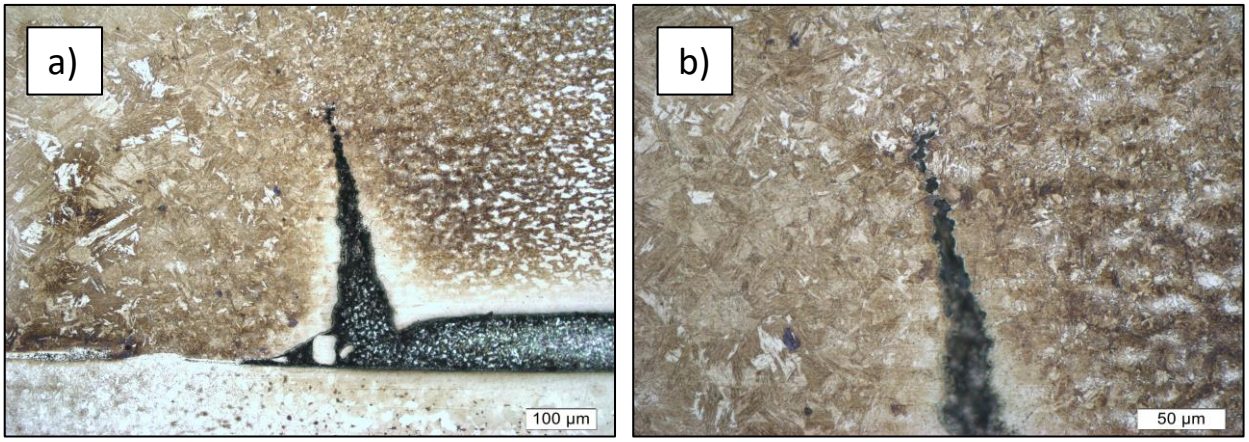

Figure 26: a) LOM micrographs (etched with 2% Nital) of cracking in the HAZ (cross-section) of the RSW joint between DP590 and Zn-coated steel shown in Figure 25a, and b) detail at higher magnification.

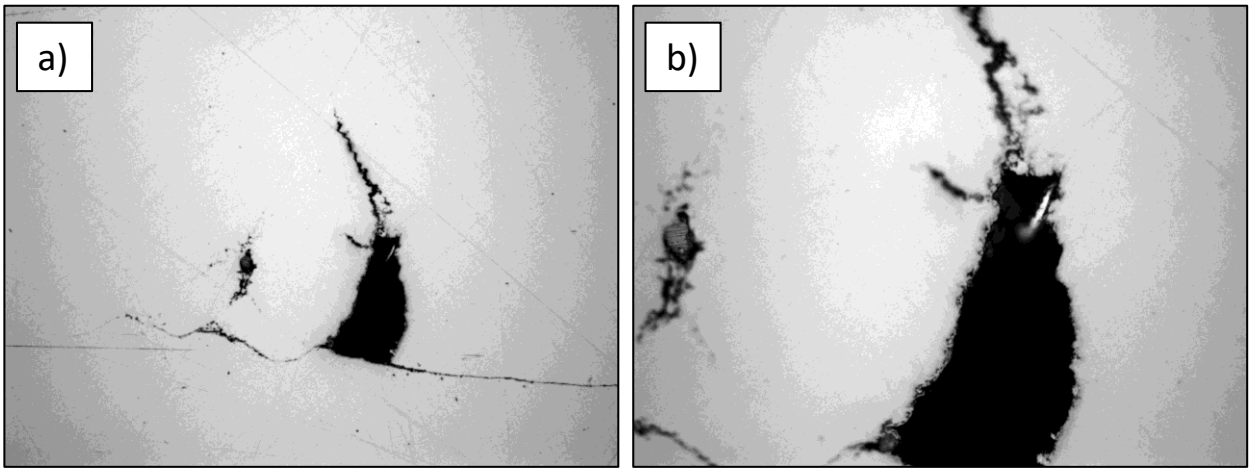

Figure 27: a) LOM micrographs (as-polished condition) of cracking in the HAZ (cross-section) of the RSW joint between DP980 and Zn-coated steel shown in Figure 25b, and b) detail at higher magnification.

Cracks were examined using SEM. BSE imaging mode was used in the SEM. Backscattered electrons are incoming electrons that hit the sample, are scattered by the electronic structure of the sample, and end up escaping from the surface. The BSE signal provides good atomic number contrast and can provide some information on local composition differences. It is especially useful when looking for zinc in the steel samples due to the difference in atomic number between zinc

and iron as per the periodic table. Zinc will have appeared brighter in BSE images as compared to the steel substrate. This can be seen in Figure 28 and Figure 29, which show the cracks in the HAZ of the DP590 and DP980 weld, respectively. In Figure 28, it can be seen that the crack faces are completely covered with zinc or a Zn-rich phase due to the contrast provided by the BSE images. In addition, penetration of zinc away from the crack along prior austenite grain boundaries can be clearly observed. Coverage of the crack faces by zinc can also be seen in Figure 29, which shows the crack tip region of this much larger crack (see Figure 27). Again, zinc penetrations ahead of the crack tip along prior austenitic grain boundaries can be clearly observed.

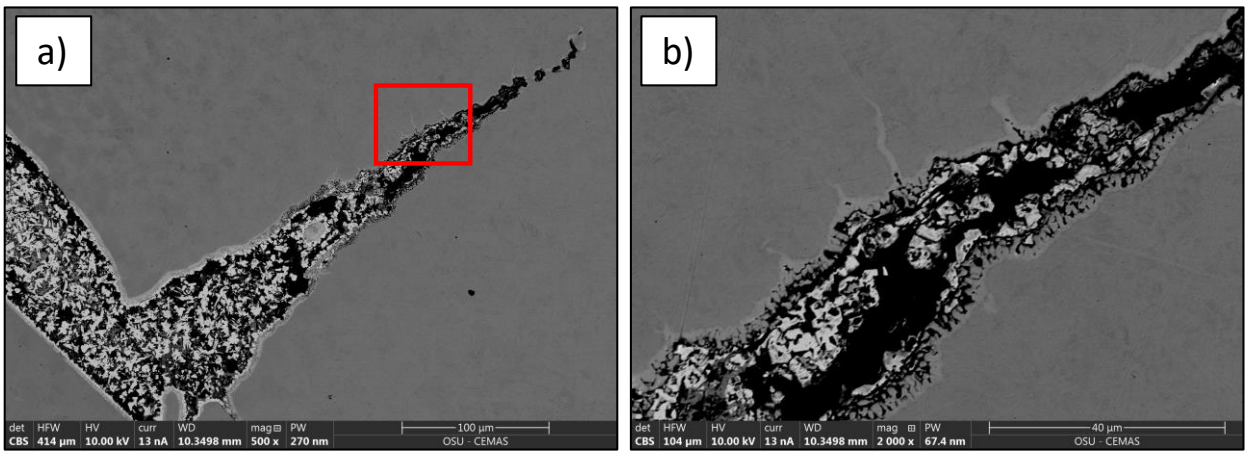

Figure 28: SEM imaging (backscattered electrons) of cracking in the HAZ of the RSW joint between DP590 and Zn-coated steel shown in Figure 25a and Figure 26, and b) detail showing complete coverage of crack faces with zinc and branching of Zn penetrations of the crack along prior austenite grain boundaries.

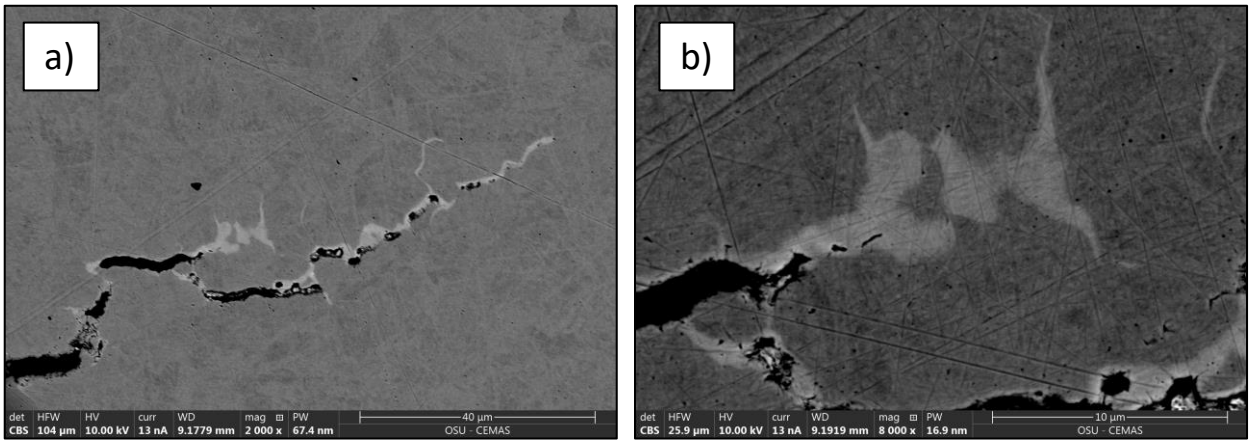

Figure 29: SEM imaging (backscattered electrons) of cracking in the HAZ of the RSW joint between DP980 and Zn-coated steel shown in Figure 25b and Figure 27, and b) detail showing zinc penetrations at the crack tip along prior austenite grain boundaries.

For further analysis, chemical composition using EDS was performed on the grain boundary penetrations seen in Figure 29b. The compositional gradient across the penetration in Figure 30 shows clear evidence of zinc enrichment ahead of the crack tip.

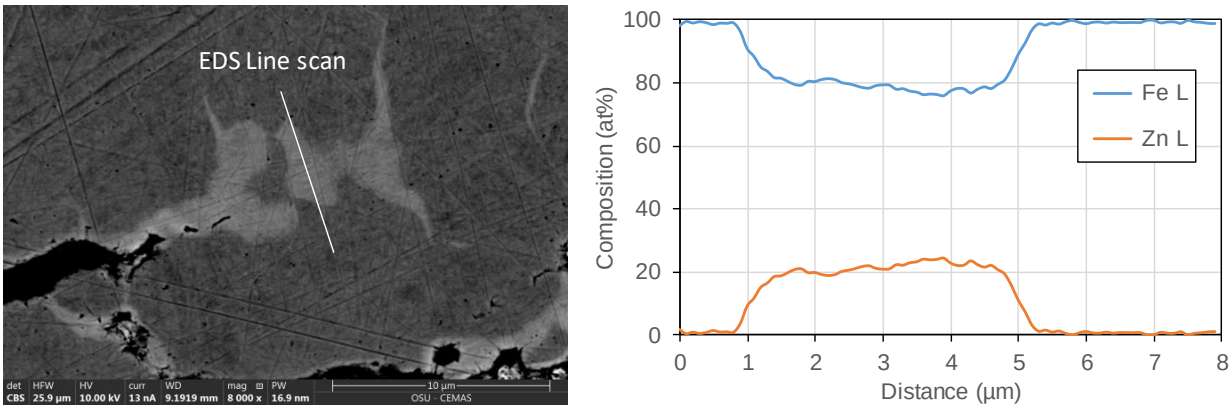

Figure 30: SEM-EDS line scan showing zinc enrichment (penetration) along prior austenite grain boundary ahead of the crack tip.

Cracking was also observed in the Usibor-1500 steel sample at the interface between the AHSS and the Zn-galvanized steel. The cracking was observed approximately 500 µm from the fusion line in the fine-grain HAZ as shown in Figure 31a. The cracking occurred only in the AHSS and not in the Zn-galvanized steel. The cracking that occurred in this sample did not open as large as in the two DP Steels, presumably as a result of the much high tensile strength of the material

(Table 3). This cracking was also intergranular in nature, forming along the prior austenite grain boundaries (see Figure 31).

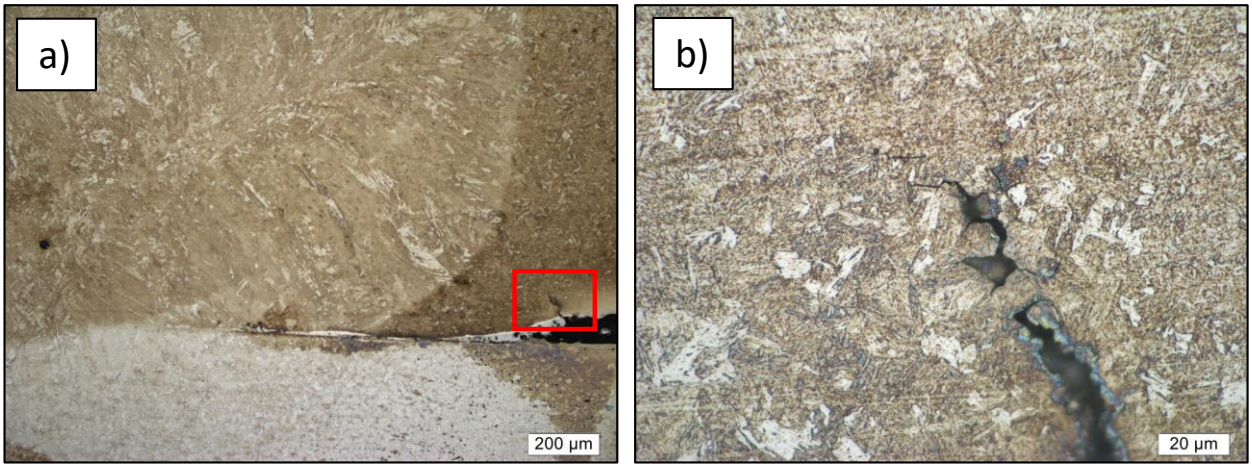

Figure 31: a) LOM micrographs (etched with 2% Nital) of cracking in the HAZ (cross-section) of the RSW joint between Usibor-1500 and Zn-coated steel shown in Figure 25c, and b) detail at higher magnification.

The cracking was then examined in the SEM using BSE imaging mode. It can be seen in Figure 32a that Zn-rich phase completely covered the fracture surface of the crack and is shown as the lighter color in comparison to the dark AHSS base material. The chemical composition gradient of the sample was determined using EDS (location as marked in Figure 32b), and verified that a Zn-rich phase is present along the crack surface and ahead of the crack tip (see Figure 33).

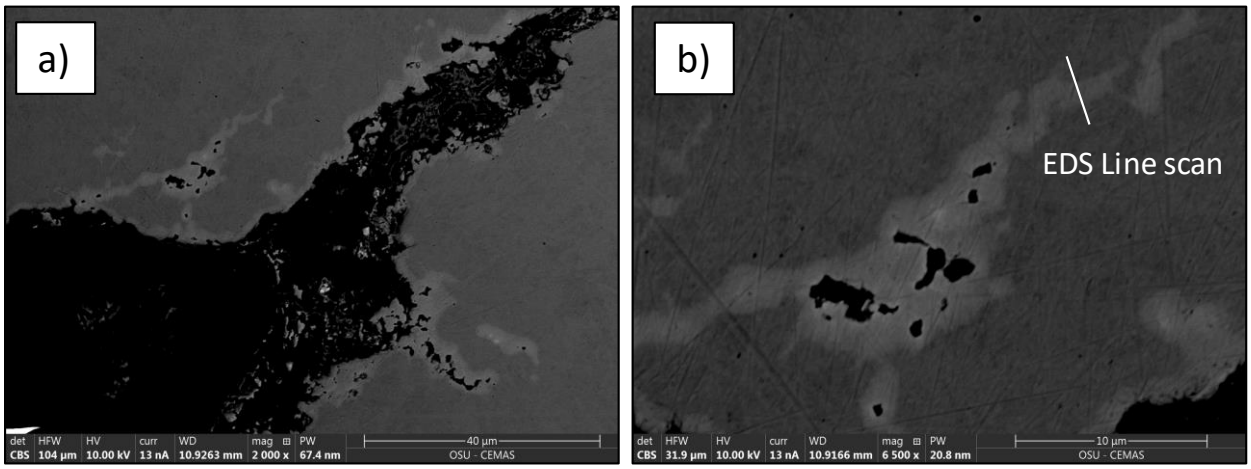

Figure 32: SEM imaging (backscattered electrons) of cracking in the HAZ of the RSW joint between Usibor-1500 and Zn-coated steel shown in Figure 25c and Figure 31 Figure 27, and b) detail showing zinc penetrations off the main crack along prior austenite grain boundaries and location of EDS line scan.

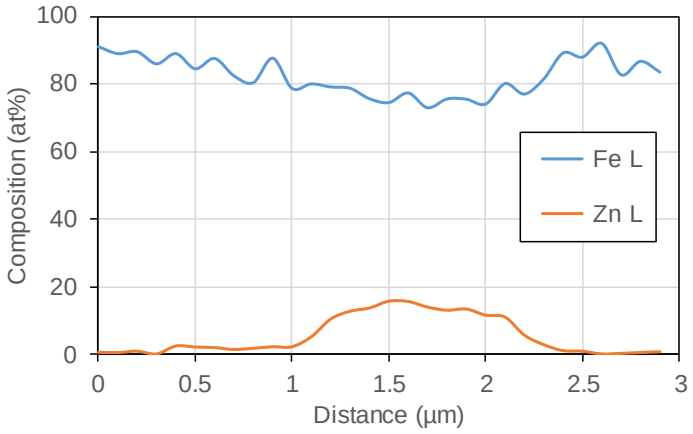

Figure 33: Compositional gradient measured using EDS along penetrated prior austenite grain boundaries shown in Figure 32b.

The SEM BSE imaging shown in Figure 34a further confirms that the crack was intergranular. There is also evidence shown in Figure 34b that the Zn-rich phase penetrated along grain boundaries away from the main crack. In some of these locations secondary cracking opened while in others cracking did not occur.

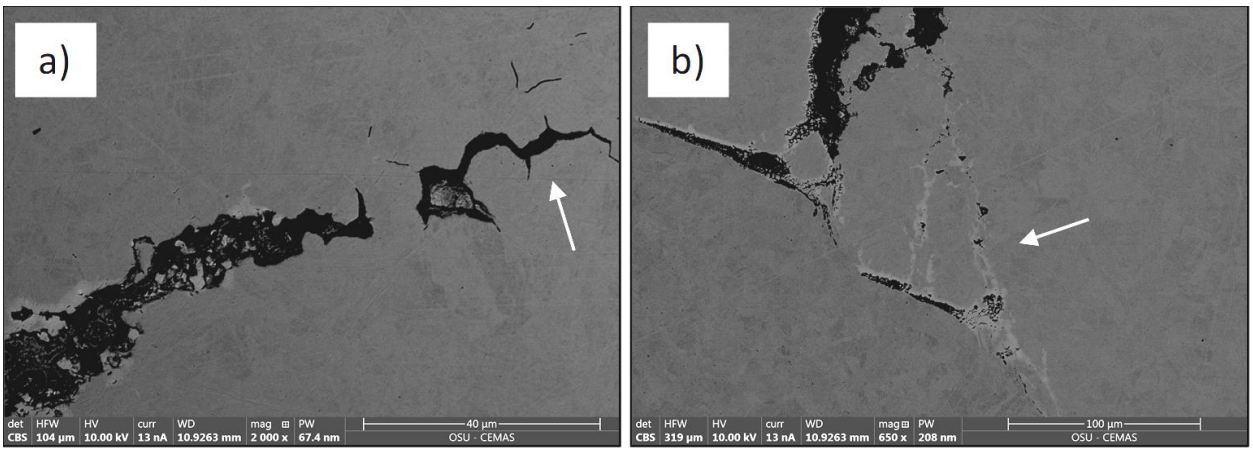

Figure 34: Further details (BSE imaging) of cracking in the HAZ of the RSW joint between Usibor-1500 and Zn-coated steel shown in Figure 25c and Figure 31Figure 27: a) Evidence of intergranular crack path at the crack tip, and b) network of penetrated grain boundaries away from the main crack.

5.3.2 Modified Electrodes Set #2 - Weld Sets #14 - #17

In the cross-section of the Usibor-1500 sample from Weld Set #14 there was also surface cracking detected in multiple locations. Cracking was found at the interface between the CU-electrode and the Zn-coated (electroplated) Usibor-1500 sheet. SEM inspection using BSE imaging mode showed the cracks as well as several penetrations containing what appeared to be Zn-rich phase that penetrated along prior austenite grain boundaries (Figure 35).

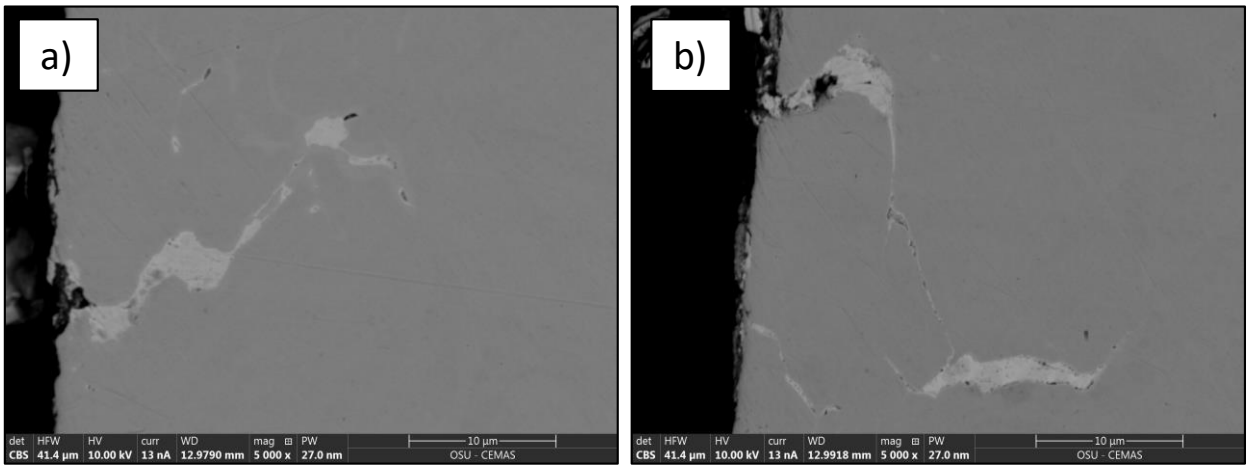

Figure 35: Surface cracks and penetrated grain boundaries in the region of the electrode indentation in the Usibor-1500 sheet.

EDS mapping was performed on one of the cracks that not only revealed the presence of a Zn-rich phase, but also a Cu-rich phase (Figure 36). This Cu is believed to come from the RSW electrodes used during welding. Copper is also known to lead to LME cracking in steels [24].

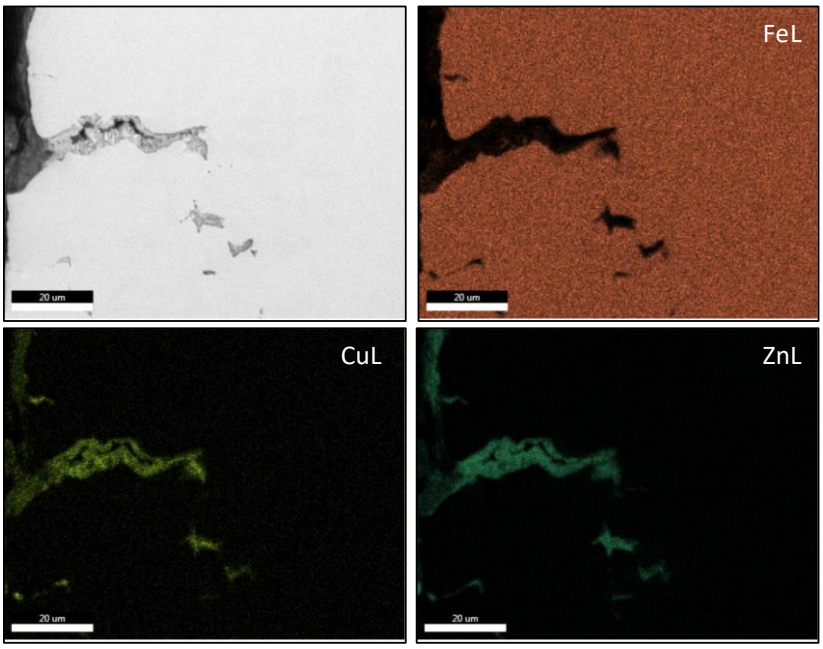

Figure 36: EDS mapping of a surface crack in the electrode indentation region of the Usibor-1500 sheet. Results show zinc and copper along the crack faces and evidence of penetration along prior austenite grain boundaries.

5.4 Materials Cooled with Liquid Nitrogen – Weld Set #6

During Weld Set #6, the samples were cooled using a liquid N bath immediately prior to being welded. The process of cooling the samples would lead to non-uniform cooling and provide additional stresses during the welding process as suggested in section 4.3.4. The three welds performed during Weld Set #6 were inspected for surface cracking both optically and using dye penetrant testing spray. Neither method revealed evidence of surface cracking. The samples were then metallographically prepared for LOM inspection. The cross-sectioning did not reveal any evidence of LME occurring.

5.5 3-Stack Weld Setup Placing Zn-Galvanized Material at Two Interfaces of AHSS – Weld Set #7

The welds performed for Weld Set #7 utilized a three-stack set up, placing the Zn-galvanized steel at two interfaces between the AHSS materials. These samples were optically inspected for surface cracking which revealed no evidence of its occurrence. The samples were the metallographically prepared for LOM examination for cracking at the interface between the AHSS and the Zn-galvanized steel. This LOM examination revealed no evidence of LME cracking at the interface.

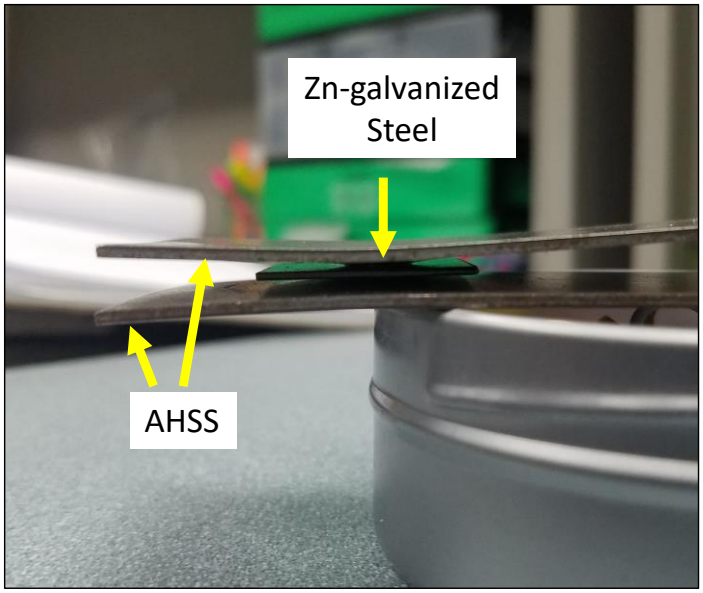

Figure 37: Result of a 3-stack weld setup for DP590 materials.

5.6 Class II Type-B Domed Electrodes Used to Provide Non-Uniform Cooling – Weld Sets #8 - #10

The use of Class II Type-B domed electrodes was utilized in Weld Sets #8 - #10 in order to provide non-uniform cooling and a unique weld geometry as suggested in section 4.3.6. After

welding these samples were optically inspected for surface cracking, which revealed no evidence of its occurrence. After surface inspection, the samples were cross-sectioned and metallographically prepared for LOM examination. During LOM examination no LME was observed at the interfaces between the AHSS and the Zn-galvanized steel samples.

5.7 External Clamping System Applying Tensile Stresses During Welding – Weld Sets #11 - #13

The last method used to induce an extreme amount of tensile stress and deformation of the sample materials during welding was using an external clamping system. This system was able to bend the samples over the bottom electrode during the welding process. Combinations of high-current – high force, high-current – low force, and low-current – high-force were utilized. After welding the samples were optically inspected for surface cracking, which revealed no evidence of its occurrence. The samples were then cross-sectioned and metallographically prepared for LOM examination. During LOM examination no evidence of LME cracking was observed.

CHAPTER 6. SUMMARY AND CONCLUSIONS

The literature review revealed that three necessary factors are required for LME cracking to occur: **1)** tensile stresses, **2)** a susceptible microstructure, and **3)** the presence of liquid metal contact. LME typically in resistance spot welds of high strength automotive steels occurs in the HAZ of the welds, where austenization of the material occurred at high temperatures during the weld thermal cycle, suggesting that austenite is the more susceptible microstructure. It has also been proven that while austenite is the more susceptible microstructure, at high enough temperatures and with enough tensile stresses, LME can occur in a ferritic microstructure. LME is observed as an intergranular cracking phenomenon. During RSW applications, it has been shown that LME can be the result of many factors including insufficient welding force, excessive welding current, misaligned electrodes, improper electrode cooling, electrode wear, and excessive sheet separation. Based on these existing approaches, one goal of this study was to use several different approaches to introduce LME during RSW of three AHSS materials in dissimilar material combination with a Zn-coated steel. Once cracking was obtained, metallurgical characterization and examination was conducted using LOM and SEM to help identify LME crack characteristics. The following conclusions was be drawn from these experiments:

Varying the welding parameters alone, in particular the welding force and the heat input, was not sufficient in reproducing LME cracking in the laboratory setting (weld sets #1 - #3). In an attempt to provide additional tensile stresses during welding, a 3-D printed fixture was used to separate the joining partners before they were forced together by the electrodes during welding (weld Set #4). This fixture proved to be strong enough to deform the joints with the two DP steels, but it failed when welding the Usibor-1500 material due to its extremely high tensile strength.

Regardless of the deformation that was introduced during the welding no LME cracking was observed. This might also be because the deformation might actually have occurred more in the Zn-coated plain carbon steel due to its lower mechanical properties. So the HAZ region of the AHSS might not have actually seen higher tensile stresses during the welding process.

In order to achieve LME cracking in the RSW joints, the use of the geometrically modified electrodes (weld sets #5 and #14) proved most successful. These electrodes were able to impose a considerable deformation to the HAZ of all three AHSS during welding, and cracking was observed in these welds both at the interface to the Zn-galvanized steel, and on the surface of the AHSS sheet at the interface to the electrode. The latter form of cracking only occurred in the Usibor-1500 steel.

The use of a liquid N bath to cool the material prior to welding (weld set #6) proved insufficient in providing non-uniform cooling during the welding process. Perhaps cooling the weld during the welding process and immediately after welding would have been more successful in inducing LME cracking. The use of Class II Type-B electrodes as a method to provide non-uniform cooling was also unsuccessful at reproducing LME cracking (weld sets #8 - #10).

The three-stack method used to place the Zn-galvanized joining partner at two interfaces between the AHSS materials also proved unsuccessful at reproducing any evidence of LME cracking. These samples additionally underwent plastic deformation by using the 3-D printed fixture. Again, this might have to do with the deformation actually occurring in the lower strength Zn-coated steel, and not in the HAZ of the AHSS materials.

Lastly, the use of the external clamping system (weld sets #11 - #13) was successful at providing tensile stresses to the AHSS materials causing plastic deformation during the welding

process. Although the deformation occurred as evident when looking at the cross sections of the samples, no evidence of LME cracking was observed during metallographic examination. Table 12 provides a summary of the welds in which LME cracking was observed in this study.

Table 12: Observation of LME cracking in this study: no LME observed (blue), and LME observed in weld cross section (green).

	Weld Set																
Material	#1	#2	#3	#4	#5	#6	#7	#8	#9	#10	#11	#12	#13	#14	#15	#16	#17
DP590					LME												
DP980					LME												
Usibor-1500					LME									LME			

The results in Table 12 need to be looked at somewhat critical. First of all, only one welded sample was performed for each AHSS material at each welding (weld set) parameter. This was due to the fact that only limited AHSS sheet material was available for this study. For statistical significance at least 3-5 welded samples would be recommended. In addition, the fact that there was no LME cracking observed in a particular weld cross-section does not necessarily mean that cracking did not occur. Due to the small nature of the LME cracking, and the method of cross-sectioning, cracks could have occurred, but might not have been exposed in the evaluated cross-section. The cracking in the HAZ may lie in a different plane that was not exposed during the metallurgical preparation. A schematic of this issue is shown in Figure 38.

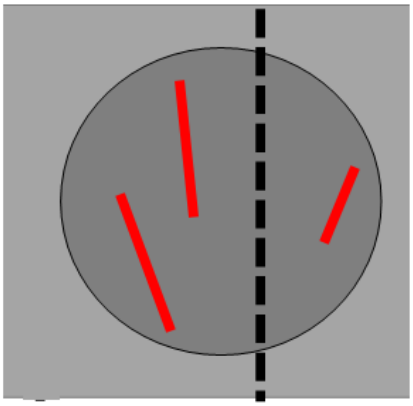

Figure 38: Schematic of cross-sectioning that would not expose LME cracking at the interface in the RSW joints.

In terms of the characteristic features of the observed LME cracking in the RSW joints, it can be noted that both the interfacial cracking and the surface cracking have a clear intergranular crack path. Some branching from the main crack was observed in some of the samples. All LME cracking that was observed occurred in the HAZ of the weld samples at a distance from the fusion line. This region experienced temperatures high enough for austenization of the material during the weld thermal cycle, and subsequent transformation to martensite during the rapid cooling in resistance spot welding. The cracking occurred in the fine grained HAZ for all three AHSS materials along prior austenite grain boundaries. BSE imaging and EDS chemical analysis in the SEM revealed for the interfacial cracking that the crack faces were covered with a Zn-rich phase. Zinc penetration along prior austenite grain boundaries was clearly visible ahead of the crack tip and as branching off the main crack. Which the interfacial cracking was associated with zinc from the Zn-coated joining partner, the observed surface cracking and penetrations at the interface of the AHSS material to the RSW electrodes showed evidence of zinc and copper inside and ahead of the cracks. These surface cracks were only found in welds on Usibor-1500. The copper is probably from the electrode material, while the zinc was in this case due an additional electroplating of the Usibor-1500 sheet prior to welding.

REFERENCES

1. Federal Register. Department of Transportation. Environmental Protection Agency. Part II, Vol. 77, No. 199, pg. 62641. October 15, 2012.

2. Tamaerlli, Carrie. *AHSS 101: The Evolving Use of Advanced High-Strength Steels for Automotive Application.* Steel Market Development Institute. https://www.autosteel.org/global/document-types/news/2012/auto---gdis-ahss-101-release?siteLocation=5b3fd1fa-9942-4f0d-8d44-91a318f668fe. 2000.

2. Keeler, Stuart. *Science of Forming*. Automotive Steels – Online Technical Resources. http://www.metalformingmagazine.com/enterprise-zones/article/?//2012/5/1/Automotive_Steels--Online_Technical_Resources. May 1, 2012.

4. *Dual Phase (DP) Steels.* World Auto Steel. https://www.worldautosteel.org/steel-basics/steel-types/dual-phase-dp-steels/.

5. *Hot-Formed (HF) Steels*. World Auto Steel. https://www.worldautosteel.org/steel-basics/steel-types/hot-formed-hf-steel/

6. *Light-weighting Lies Heavy on Automotive Industry.* Auto Components India. http://autocomponentsindia.com/lightweighting-lies-heavy-on-automotive-industry/

7. Phillips, David. *Introduction to Welding Engineering.* Chapter 3 Resistance Welding Processes. Pg. 86. 2016.

8. Frei, Julian, and Rethmeier, Michael. *Susceptibility of Electrolytically Galvanized Dual-Phase Steel Sheets to Liquid Metal Embrittlement During Resistance Spot Welding.* Welding in the World. Volume 62, Issue 5, pg. 1031-1037. 2017.

9. Kamdar, M.H. *Liquid Metal Embrittlement.* Treatise on Materials Science & Technology. Volume 25, pg. 361-459. 1983.

10. Takahashi, M., Nakata, M., Imai, K., Kojima, N., and Otsuka, N. *Liquid Metal Embrittlement of Hot Stamped Galvannealed Boron Steel Sheet – Effect of Heating Time on Crack Formation.* ISIJ International. Volume 57, Issue 6, pg. 1094-1101. 2017.

11. Tolf, E., Hedegard, J., and Melander, A. *Surface Breaking Cracks in Resistance Spot Welds of Dual Phase Steels with Electrogalvanised and Hot Dip Zinc Coating.* Science and Technology of Welding and Joining. Volume 18, Issue 1, pg. 25-31. 2013.

12. Jung, G., Woo, I., Suh, D., and Kim, S. *Liquid Zn Assisted Embrittlement of Advanced High Strength Steels with Different Microstructures.* Metals and Materials International. Volume 22, Issue 2, pg. 187-195. 2015.

13. Nicholas, M. G., and Old, C. F. *Review: Liquid Metal Embrittlement.* Journal of Materials Science. Volume 14, Issue 1, pg. 1-18. 1979.

14. Vermeersch, M., De Waele, W., and Van Caenegem, N. *LME Susceptibility of Galvanised Welded Structures of High Strength Steels.* Sustainable Construction and Design. Conference, pg. 442-447. 2011.

15. Fernandes, P., Jones, D. *Mechanisms of Liquid Metal Induced Embrittlement.* International Materials Review. Volume 42, Issue 6, pg. 251-261. 1997.

16. Sigler, D., Schroth, J., Yang, W., and Gayden, X. *Observations of Liquid Metal-Assisted Cracking in Resistance Spot Welds of Zinc-Coated Advanced High-Strength Steels.* Steel Metal Welding Conference XIII. Pg, 1-17. 2008.

17. Lee, C., Fan, D., Sohn, R., Lee, S., and Cooman, B. *Liquid-Metal-Induced Embrittlement of Zn-Coated Hot Stamping Steels.* The Minerals, Metals, & Materials Society and ASM International. 2012.

18. Gaul, H., Brauser, S., Weber, G., and Rethmeier, M. *Methods to Obatin Discontinuities in Spot-Welded Joints Made of Advanced High-Strength Steels.* Welding in the World. Vol. 55, pg. 99-106. 2011.

19. Ma, C., Chen, D., Bhole, S., and Boudreau, G. *Microstructure and Fracture Characteristics of Spot-Welded DP600 Steel.* Materials Science and Engineering: A. 485. 334-346. 10.1016/j.msea.2007.08.010.2007.

20. Brooks, R. *Accepting the Challenge of Welding UHSS.* Welding Design and Fabrication (Online). Pg. 1-2. 2013.

21. Ande, O., Ighodaro, R., Biro, E., and Zhou, N. *Study and Applications of Dynamic Resistance Profiles During Resistance Spot Welding of Coated Hot-Stamping Steels.* The Minerals, Metals, and Materials Society and ASM International. Vol. 48A. Pg. 745-758. DOI: 10.1007/s11661-016-3899-3. 2016.

22. Kim, Y., Kim, I., Kim, J., Chung, Y., and Choi, D. *Evaluation of Surface Cracks in Resistance Spot Weld of Zn-Coated Steel*. Materials Transactions. Vol. 55 No.1, pg. 171-175. 2013.

23. Ashiri, R., Haque, M., Ji, C., Shamanian, M., Salimijazi, H., and Park, Y. *Supercritical Area and Critical Nugget Diameter for Liquid Metal Embrittlement of Zn-Coated Twinning Induced Placticity Steels.* Scripta Materialia. 109. 6-10.10.1016/j.scriptamat.2015.07.006. 2015.

24. Lippold, John. *Welding Metallurgy and Weldability.* Pg. 20-207. 2015.